

UCSF

UC San Francisco Electronic Theses and Dissertations

Title

Building the Machine of Life: From Simple Tubulin Building Blocks to the Complex Architecture of the Mitotic Spindle

Permalink

<https://escholarship.org/uc/item/1290p6x0>

Author

Richter, Manuela

Publication Date

2024

Supplemental Material

<https://escholarship.org/uc/item/1290p6x0#supplemental>

Peer reviewed|Thesis/dissertation

Building the Machine of Life: From Simple Tubulin Building Blocks to the Complex
Architecture of the Mitotic Spindle

by
Manuela Richter

DISSERTATION
Submitted in partial satisfaction of the requirements for degree of
DOCTOR OF PHILOSOPHY

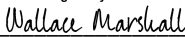
in

Cell Biology

in the

GRADUATE DIVISION
of the
UNIVERSITY OF CALIFORNIA, SAN FRANCISCO

Approved:

DocuSigned by:

43941FCFA7C0447... Wallace Marshall
Chair

DocuSigned by:

DocuSigned by: Orion Weiner

DocuSigned by:

DocuSigned by: David Agard

DocuSigned by:

8305715E0D454DC... Sophie Dumont

Committee Members

Copyright 2024

by

Manuela Richter

Acknowledgments

I am extraordinarily grateful for the mentorship, leadership, compassion, and scientific prowess of Sophie Dumont. Her dedication to rigorous science, compelling science communication, and justice in the scientific community is inspiring. Sophie's acuity and big-picture focus on what makes an interesting scientific question have transformed my abilities as a scientist.

I am grateful to the accomplished and collaborative scientists that are in the Dumont lab for their incredible feedback and support: Miquel Rosas Salvans, Megan Chong, Nathan Cho, Vanna Tran, Caleb Rux, Zack Mullin-Bernstein, Maddie Blaaw, Sterre van Wierst, and Jinghui Tao, as well as the brilliant and selfless scientists who have come from this lab: Lila Neahring, Carly Garrison, Renaldo Sutanto, Pooja Suresh, Andrea Serra Marques, Alex Long, Ronja Houtekamer, Jonathan Kuhn, Christina Hueschen, and Mary Elting. I also thank Toni Hurley, Tiffany Criger, Veena Mohan, Steve Ha, and Danh Le for their support.

I thank the greater UCSF community for their continuous valuable feedback and engagement with my science: Orion Weiner, Wallace Marshall, David Agard, Fred Chang, Barbara Panning, Seemay Chou, Geeta Narlikar, Kaveh Ashrafi, David Booth, Arthur Molines, Catherine Tan, Joël Lemièrre, Paula Real, Anne Pipathsouk, Jason Town, Tamas Nagy, Rachel Brunetti, and Ben Larson, as well as those from the broader science community: Thomas Surrey, Dan Needleman, Trina Schroer, Dick

McIntosh, and Nicole King for helpful discussions and mentorship. I thank Dr. MJ Whitehouse for her generosity and support during my PhD.

I am grateful for the tenacious support and unbridled laughter from Amanda and Brendan (and Halley and Nova), as well as the relentless strength and support of my classmates: in particular, Natalie and Lesya, Gabby, Henry, Ben, and Clara. I am thankful to the lifetime love and support of Crumplebottom's Llamas: Amelia and Adrian, Ava, Laura (and Lulu), and Margaret, and to my friends who've always inspired me to be the best version of myself: Mindy, Jeff, Ashley, Renata, Ben-han, and Roberto. I am grateful to my ultimate frisbee team Tempo for teaching me to shout out the positive.

I thank my friends from Woods Hole for rekindling my childlike sense of wonder in science: in particular, Chunzi, Cynthia, Gil, Jana, Luci, Mugdha, Nick, Rafael, Sid, Yahor, and Zoë for the late nights, sweat, tears, microscopy oil, and squid ink.

I thank my family for their unwavering love and intellectual support: in particular, my tío Juan Pablo Sanz, as well as my parents Cristina and Hans Jürgen Richter who sacrificed everything, including their time, career, and home countries, for me.

Contributions

Chapters 1, 2, and 4 are from the following published manuscript.

Manuela Richter, Lila Neahring, Jinghui Tao, Renaldo Sutanto, Nathan H Cho, Sophie

Dumont (2023) **Kinetochores-fiber lengths are maintained locally but**

coordinated globally by poles in the mammalian spindle *eLife* 12:e85208.

<https://doi.org/10.7554/eLife.85208>

I, Manuela Richter, designed and conducted experiments, performed data analysis, made figures, and wrote the paper under the guidance of Sophie Dumont. Lila Neahring and Nathan H Cho contributed to the generation of the p50 lentivirus, imaging of spindle formation in p50 overexpression, and imaging of p50 overexpression in human cells. Jinghui Tao and Renaldo Sutanto contributed to image analysis, as well as the autocorrelation analysis.

Chapter 3 is unpublished work from a collaboration between myself, Zack Mullin-Bernstein, and Caleb Rux under the guidance of Sophie Dumont. I designed experiments, performed data analysis, made figures, and wrote the thesis manuscript. Zack Mullin-Bernstein performed the microneedle experiments in collaboration with me. Caleb Rux provided expertise during data analysis and interpretation.

Building the Machine of Life: From Simple Tubulin Building Blocks to the Complex Architecture of the Mitotic Spindle

Manuela Richter

Abstract

How nature builds complex and beautiful architecture from very simple building rules and building blocks is a fascinating biological question. During every cell division, nanometer-scale components self-organize to build a micron-scale spindle. In mammalian spindles, microtubule bundles called kinetochore-fibers attach to chromosomes and focus into spindle poles. Despite evidence suggesting that poles can set spindle length, their role remains poorly understood. In fact, many species do not have spindle poles. Here, we probe the pole's contribution to mammalian spindle length, dynamics, organization, and function by inhibiting dynein to generate spindles whose kinetochore-fibers do not focus into poles, yet maintain a metaphase steady-state length. We find that unfocused kinetochore-fibers have a mean length indistinguishable from control, but a broader length distribution, and reduced length coordination between sisters and neighbors. Further, we show that unfocused kinetochore-fibers, like control, can grow back to their steady-state length if acutely shortened by drug treatment or laser ablation: they recover their length by tuning their end dynamics, albeit slower due to their reduced baseline dynamics. Thus, kinetochore-fiber dynamics are regulated by

their length, not just pole-focusing forces. Next, we probe force-induced displacement of kinetochore-fibers lacking pole-focusing forces to reveal hints about mechanisms underlying kinetochore-fiber anchorage and organization. Finally, we show that spindles with unfocused kinetochore-fibers can segregate chromosomes but fail to correctly do so. We propose that mammalian spindle length emerges locally from individual k-fibers while spindle poles globally coordinate k-fibers across space and time.

Table of Contents

Introduction	1
Chapter 1. Kinetochore-fiber length regulation in the mammalian spindle	4
Introduction	4
Results	7
<i>Spindle poles coordinate but do not maintain kinetochore-fiber lengths</i>	7
Figures	12
Supplemental Figures	15
Chapter 2. Dynamics and length regulation in kinetochore-fibers	20
Introduction	20
Results	20
<i>Kinetochore-fibers recover their lengths without focused poles</i>	20
<i>Kinetochore-fibers exhibit reduced end dynamics in the absence of poles and pole-focusing forces</i>	22
<i>Kinetochore-fibers tune their end dynamics to recover length, without pole-focusing forces</i>	23
Figures	25
Supplemental Figures	31
Chapter 3. Probing kinetochore-fiber anchorage	36
Introduction	36

Preliminary Results	38
<i>Kinetochore-fibers recover displacement from force applied at short</i>	
<i>timescales regardless of poles.....</i>	38
<i>Unfocused kinetochore-fibers exhibit permanent displacement at long</i>	
<i>timescales of force applied compared to control.....</i>	39
<i>Kinetochore-fiber relaxation can be quantified temporally and spatially.....</i>	40
Figures	43
Supplemental Figures	46
Discussion and Outlook	47
Chapter 4. Functional coordination of kinetochore-fibers in the	
mammalian spindle.....	55
Introduction	55
Results	55
<i>Spindle poles coordinate chromosome segregation and cytokinesis</i>	55
Figures	57
Supplemental Figures	59
Discussion.....	60
Figures	65
Materials and Methods	67
Cell biology and microscopy	69
Cell culture	69

Lentiviral plasmids and cell line construction	70
Imaging	70
Photobleaching and laser ablation (Figure 2,3,4)	71
Nocodazole washout (Figure 2)	72
Reversine treatment (Figure 6)	73
Microneedle manipulation (Figure 5)	73
Image analysis and statistics	73
Image analysis	73
Spindle major and minor axes length (Figure 1D, Figure supplement 4)	73
K-fiber length (Figure 1,2, Figure supplement 4B,C)	74
Spatial correlation analysis (Figure supplement 6)	75
Tracking photobleach marks along k-fibers (Figure 3, 4)	77
Displacement calculations (Figure 5)	77
Exponential curve fitting (Figure 5)	78
Log axis transformation and linear regression (Figure 5)	79
Cell division analysis (Figure 6)	79
Statistical analysis	79
Autocorrelation (Figure 3A)	80
Script packages	80
Video preparation	81
References	82

List of Figures

Figures

Figure 1. Spindle poles coordinate but do not maintain kinetochore-fiber lengths.	13
Figure 2. Kinetochore-fibers recover their lengths without focused poles.	26
Figure 3. Kinetochore-fibers exhibit reduced end dynamics in the absence of poles and pole-focusing forces.....	28
Figure 4. Kinetochore-fibers tune their end dynamics to recover length, without pole-focusing forces.....	30
Figure 5. Kinetochore-fibers recover displacement from forces applied at short timescales, but permanently displace at longer timescales in the absence of poles and pole-focusing forces.....	44
Figure 6. Spindle poles coordinate chromosome segregation and cytokinesis... 	58
Figure 7. Spindle length is a local spindle property and length coordination is a global spindle property.....	66

Supplemental Figures

Figure supplement 1. High cytoplasmic p50 intensity correlates with unfocused spindles.	15
Figure supplement 2. Interkinetochore distance is preserved in unfocused spindles.	16
Figure supplement 3. p50 overexpression in RPE1 cells generates unfocused spindles.	17
Figure supplement 4. Length measurement methods.	17
Figure supplement 5. Centrosome radius approximation.	18
Figure supplement 6. Kinetochores-fiber lengths are spatially correlated in control but not unfocused spindles.	18
Figure supplement 7. Kinetochores-fiber lengths before ablation.	33
Figure supplement 8. Minus-end depolymerization resumes after length recovery following ablation.	34
Figure supplement 9. Log transformation of axes and linear regression describes k-fiber relaxation curves.	46

Videos

Video 1. Control spindle assembly in the presence of pole-focusing forces.	15
Video 2. Spindle assembly with inhibited pole-focusing forces.	15
Video 3. Kinetochores-fiber lengths over time in metaphase: control vs unfocused spindle.	15

Video 4. Ablating kinetochore-fibers: control vs unfocused spindle.	31
Video 5. Spindle assembly after nocodazole washout:	
control vs unfocused spindle.	31
Video 6. Photobleaching kinetochore-fibers to measure microtubule flux:	
control vs unfocused spindle.	32
Video 7. Ablating and photomarking kinetochore-fibers:	
control vs unfocused spindle.	32
Video 8. Photobleaching control kinetochore-fibers after ablation	
and length recovery.	32
Video 9. A reversine-treated control spindle undergoing anaphase:	
control vs unfocused spindle.	59

List of Tables

Table 1. Key resources used in this work.	67
---	-----------

Introduction

How nature is able to build complex and beautiful architecture from very simple building rules and building blocks is a fascinating biological question. How does a tiny seed turn into a tall flower that knows to grow its roots into the ground and its stem into the sky? How does a flock of birds coordinate changes in its movement like a single entity on timescales faster than any single bird can react? How does the hair on our heads know to be longer than the hair on our arms? In this dissertation, I will investigate fundamental building rules based on dynamics, spatial coordination, and self-organization of building blocks to generate the structure responsible for propagating life - the mitotic spindle.

During cell division, cells rely on their mitotic spindle to robustly and accurately separate their genetic material into two new cells. First, DNA is duplicated and densely packaged into pairs of chromatids called chromosomes. These chromosomes align in the center of the dividing cell, where they are physically pulled apart into the two new cells. The mitotic spindle is the structure that physically attaches to and moves these chromosomes to their correct locations. Defects in spindle attachment, positioning, and architecture can lead to missegregation of chromosomes, where the two new cells do not receive the correct genetic information. These errors are often associated with developmental disorders, cancer, and cell death. So how do cells make sure their mitotic spindle gets built flawlessly every time to perfectly divide their chromosomes?

We know many individual parts that are required for building the mitotic spindle and fine-tuning its architecture, attachments, and dynamics, but it is not known how they

all work together. For example, many proteins are known to tune spindle length, but the guiding principles for how spindles set and regulate their length is unclear, though some hints are known. Positioned at either end of the spindle - where chromosomes end up after dividing - is a structure called the spindle pole. Poles hold on to and cluster the spindle fibers connected to chromosomes, so they are an enticing model for globally regulating spindle length, dynamics, and anchorage. However, individual spindle fibers can self-repair, growing back and reincorporating into the pole if severed with a high-powered precise laser. What spindle properties are set globally by poles and what individual spindle fibers can do locally on their own is not known. How do spindle poles contribute, if at all, to setting spindle fiber length, dynamics, and anchorage? In this dissertation, I will answer this question using molecular, biophysical, and microscopy tools to understand how spindles are built.

Here, we probe length regulation, dynamics, and coordination of mitotic mammalian spindles at metaphase using advanced biological tools to understand how they are self-organized. We imaged rat kangaroo cells called PtK2, a cell type often used in mitotic research due to their flatness and low number of chromosomes, making their spindles easy to image. To visualize components of the spindle, we use fluorescence microscopy, where cell proteins are tagged using an excitable fluorescent marker. For example, we genetically engineer cells to express GFP-tubulin - the main building block of the spindle genetically attached to a green fluorescent protein. Furthermore, we use advanced biophysical tools such as laser ablation, photobleaching, and microneedle manipulation. Laser ablation uses a nanosecond-pulsed laser to deliver precise but powerful bursts of energy capable of destroying

regions on spindle fibers, effectively severing them. We can then track how these cut fibers grow back over time. The same laser can be used at a lower power to locally bleach fluorescent markers, which can be used to track dynamics of the bleached regions over time, especially while they're remodeling. Finally, microneedle manipulation uses a precise glass needle lowered into cells (not piercing cells - the cell membrane wraps around it), applying forces to spindle components and displacing them. Testing the spindle's response to force reveals underlying mechanisms of anchorage, organization, and material properties of spindles.

Our work reveals key insight into how the structure responsible for propagating life uses simple building blocks, combined with local and global rules of self-organization, to robustly build the mitotic spindle. We show that individual spindle components are able to locally regulate their own length, dynamics, and short-term anchorage, but they are still globally coordinated, homogenized, and organized by spindle poles. We propose that this represents a useful blueprint for understanding how nature build complex structures – understanding what aspects of architecture emerge locally from individual building blocks, and what aspects emerge globally from forces that coordinate the whole system – to make robust, complex, and beautiful structures across biology.

Chapter 1. Kinetochore-fiber length regulation in the mammalian spindle

Introduction

Living systems use simple, small-scale components to build larger and more complex structures. One such structure is the micron-scale spindle, built from nanometer-scale tubulin molecules. The length of the spindle dictates the distance over which chromosomes segregate in dividing cells, and spindle length is known to scale with cell size during development (Good et al., 2013; Hazel et al., 2013; Lacroix et al., 2018; Rieckhoff et al., 2020; Wühr et al., 2008). Defects in spindle length are linked to impaired chromosome segregation (Goshima et al., 1999), cytokinesis errors (Dechant and Glotzer, 2003), and asymmetric division defects (Dudka et al., 2019; Dumont et al., 2007), and long spindles have been hypothesized to come at an energetic cost (Dumont and Mitchison, 2009b). While we know many proteins that can modulate the spindle's length (Goshima and Scholey, 2010), how they work together to set spindle length and ensure robust chromosome segregation remains poorly understood. We do not know which aspects of spindle length and dynamics are regulated by global cues at the level of the whole spindle, and which are more locally regulated at the level of its components.

Mammalian spindles are built from a network of microtubules, including discrete bundles of microtubules connecting chromosomes to poles. These bundles, called kinetochore-fibers (k-fibers), are made of many microtubules, some of which directly

extend from kinetochores to poles (Kiewisz et al., 2022; McDonald et al., 1992; O'Toole et al., 2020). Poles are the convergence points of k-fiber microtubules and other microtubule minus-ends, and they can also serve as an anchor point for centrosomes, if present, and astral microtubules. In many systems, dynein and other motors work together to focus microtubules into asters and poles (Compton, 1998; Goshima et al., 2005a; Heald et al., 1996; Merdes et al., 1996; Roostalu et al., 2018; So et al., 2022). In mammals, k-fiber microtubules turn over on the order of minutes (Gorbsky and Borisy, 1989), detaching from kinetochores and getting replaced. They also exhibit poleward flux, where k-fiber tubulin moves towards poles, with k-fiber plus-ends on average polymerizing and minus-ends appearing to depolymerize at poles (Mitchison, 1989). Both biochemical factors (Goshima and Scholey, 2010) and mechanical force (Akiyoshi et al., 2010; Dumont and Mitchison, 2009a; Nicklas and Staehly, 1967) are thought to tune k-fiber dynamics at both microtubule ends and thereby tune k-fiber length. Microtubule dynamics regulators with length-dependent activities (Dudka et al., 2019; Mayr et al., 2007; Stumpff et al., 2008; Varga et al., 2006) could in principle give rise to the k-fiber's length scale, beyond simply tuning length. However, k-fiber architecture and organization vary across species, adding complexity to our understanding of how k-fibers set their length. Some spindles, such as in land plants, do not have focused poles (Yamada and Goshima, 2017), and in many species, spindles are composed of short, tiled microtubules indirectly connecting chromosomes to poles (Brugués et al., 2012; Yang et al., 2007), unlike mammalian k-fibers. Broadly, it remains poorly understood which of the mammalian spindle's emergent properties—such as length, dynamics, and

function—emerge globally from the whole spindle, or locally from individual k-fibers themselves.

While we know that perturbations that affect spindle pole-to-pole distance also affect k-fiber length, and vice versa (Waters et al., 1996), it is still unclear which sets the other. For example, global forces such as cell confinement pulls on poles, leading to k-fiber elongation by transiently suppressing apparent minus-end depolymerization (Dumont and Mitchison, 2009a), but pole-less k-fibers do not elongate under these forces (Guild et al., 2017). Similarly, locally pulling on a k-fiber with a microneedle causes it to stop depolymerizing at its pole and thus elongate (Long et al., 2020). Since poles serve as a connection point for spindle body microtubules, centrosomes, and astral microtubules, they can in principle help integrate physical and molecular information from within and outside the spindle. Indeed, one proposed model is that force integration at spindle poles sets mammalian k-fiber length and dynamics (Dumont and Mitchison, 2009b). However, focused poles may not be essential for setting spindle length, as species without focused poles (Yamada and Goshima, 2017) can still build spindles and set their length. Similarly, inhibiting dynein unfocuses poles but spindles still form albeit with altered lengths in *Drosophila* (Goshima et al., 2005b) and *Xenopus* (Gaetz and Kapoor, 2004; Heald et al., 1996; Merdes et al., 1996), and without a clear effect on mammalian spindle length (Guild et al., 2017; Howell et al., 2001). Further, it is possible to alter kinetochores and microtubule dynamics to shorten k-fibers without a corresponding decrease in the spindle's apparent length (DeLuca et al., 2006). The role of the mammalian spindle pole on k-fiber structure, dynamics, and function remains an open question.

Here, we ask which emergent properties of mammalian k-fibers require a focused spindle pole. We inhibit pole-focusing forces and ask how k-fiber length, dynamics, and function change when the spindle reaches an unfocused steady-state. Using live imaging, we find that k-fibers can set their mean length without poles but need poles to homogenize and coordinate their lengths between k-fibers.

Results

Spindle poles coordinate but do not maintain kinetochore-fiber lengths

To test whether k-fiber length is set locally or globally, we generated metaphase spindles without focused poles, but with a steady-state length at metaphase. To do so, we overexpressed the dynactin subunit p50 (dynamitin) in PtK2 mammalian rat kangaroo cells, a system with few chromosomes and clearly resolved individual k-fibers. p50 overexpression dissociates the dynactin complex and inhibits the pole-focusing forces of its binding partner, dynein (Echeverri et al., 1996; Howell et al., 2001; Quintyne et al., 1999), unfocusing poles in species such as *Xenopus* and *Drosophila* (Gaetz and Kapoor, 2004; Sharp et al., 2000). Indeed, we found that unfocused spindles correlated with higher mean intensity levels of p50 expression (**Figure supplement 1**), consistent with prior work showing mild pole disruption versus severe unfocusing depending on the severity of dynein inhibition (Elting et al., 2017; Gaglio et al., 1997, p. 199; Hueschen et al., 2019, 2017; Sharp et al., 2000, p. 200; Toorn et al., 2022). To probe the role of poles on global and local spindle architecture, here we selected unfocused spindles that maintained a steady-state structure on the minutes timescale, holding their shape over time (**Video 3**).

We first imaged unfocused spindle assembly in cells overexpressing p50 using long-term confocal fluorescence live imaging with a wide field of view to capture these rare events. While k-fibers seemed initially focused in these cells, these k-fibers eventually lost their connection to centrosomes and became unfocused, exhibiting a similar phenotype to spindle assembly in some NuMA-disrupted cells (**Figure 1A, Videos 1,2**, Silk et al., 2009). We observed disconnected centrosomes seemingly move around freely in cells with unfocused spindles (**Videos 2,3**). The resulting metaphase spindles were barrel-shaped with bi-oriented chromosomes, and they underwent anaphase after several hours instead of about 30 minutes in control, consistent with dynein inhibition at kinetochores causing an anaphase delay (Howell et al., 2001; **Figure 1A, Videos 1,2**). While these spindles had no clear poles, we sometimes observed transient clustering of neighboring k-fibers, likely due to residual pole-focusing forces from other minus-end motors or incomplete dynein inhibition. Their interkinetochore distance was indistinguishable from control (**Figure supplement 2**), suggesting that k-fibers are still under some tension from other forces (Elting et al., 2017; Kajtez et al., 2016; Maiato et al., 2004; Milas and Tolić, 2016), despite not being connected to poles. p50 overexpression in human RPE1 cells led to similar unfocusing phenotypes (**Figure supplement 3**), but k-fibers were not individually resolvable. Thus, we chose to work with p50 overexpression in PtK2 spindles and hereafter refer to these spindles and k-fibers without distinct poles and with reduced pole-focusing forces as “unfocused”.

To measure k-fiber lengths more accurately, we imaged control and unfocused spindles at metaphase using short-term confocal fluorescence live imaging at higher

spatial resolution (**Figure 1B**). If poles do not contribute to k-fiber length, we expect no change in k-fiber length distributions in unfocused spindles (**Figure 1Ci**). If poles are required to set spindle length, we expect k-fibers with a different mean length in unfocused spindles (**Figure 1Cii**). If poles merely coordinate lengths, we expect k-fibers with a greater variability of lengths in p50 spindles, but the same mean length (**Figure 1Ciii**). We first observed that in unfocused spindles, k-fibers were more spread out in the cell, with spindles covering a larger area compared to control along both its major and minor axes (**Figure 1D, Figure supplement 4A**). This is consistent with pole-focusing forces providing contractile forces to compact the spindle (Hueschen et al., 2019). Next, we measured k-fiber lengths in 3D (**Figure supplement 4B,C**). For control spindles whose k-fibers end at centrosomes at this resolution, we subtracted the radius of the centrosome ($0.97 \pm 0.10 \mu\text{m}$) from the region of measured tubulin intensity (**Figure supplement 5**). Mean k-fiber length in an unfocused spindle ($7.81 \pm 2.52 \mu\text{m}$) was not significantly different than control ($8.01 \pm 1.76 \mu\text{m}$) (**Figure 1E**). Thus, k-fibers do not require a pole connection to keep their mean length. However, these unfocused spindles showed a greater standard deviation in lengths, so we compared average k-fiber lengths per cell to account for cell-to-cell variability: the mean k-fiber length within each cell was indistinguishable between control and unfocused cells (**Figure 1F**), but the standard deviation was significantly greater in unfocused cells (**Figure 1G**). This indicates that spindle poles act to synchronize lengths between neighbors within a spindle, rather than to set and keep length. K-fibers can maintain their average length without poles, but they do so with a greater length variability.

In principle, this greater k-fiber length variability in unfocused spindles could not only come from greater length variability between k-fibers in a given cell (**Figure 1G**), but also from greater variability over time for each k-fiber. To test this idea, we measured k-fiber lengths over time (**Figure 1H, Video 3**). We observed indistinguishable mean lengths averaged over time in unfocused and control k-fibers and a greater coefficient of variation in unfocused k-fiber lengths over time compared to control (**Figure 1I, J**). Thus, while unfocused k-fibers still establish and maintain their mean lengths at a similar length scale (**Figure 1F, I**), their lengths are more variable within a cell (**Figure 1G**) and over time (**Figure 1J**) compared to control.

To test the role of poles in coordinating lengths within the spindle across space, we tested whether k-fiber length correlated with k-fiber spatial positioning within the spindle. Based on geometry and previous observations, we expected outer k-fibers to be longer than inner k-fibers in focused spindles (Kiewisz et al. 2022). This was indeed the case in control spindles, but this difference was lost in unfocused spindles (**Figure supplement 6A**). Furthermore, we expected k-fiber length to correlate with distance to the metaphase plate – k-fibers are shorter if attached to under-aligned chromosomes and longer if attached to over-aligned chromosomes (Wan et al., 2012). Here too, a correlation between k-fiber length and alignment was observed in control but it was negligible in unfocused spindles (**Figure supplement 6B**). Thus, poles coordinate k-fiber lengths spatially in the spindle to maintain its shape despite geometric constraints.

Finally, to test the role of poles in coordinating lengths within the spindle across time, we compared sister k-fiber lengths over several minutes. During chromosome oscillations, sister k-fiber lengths are normally anti-correlated (Wan et al., 2012). Indeed,

in control cells we observed that as one sister k-fiber shortened, the other elongated to maintain a constant sum of their lengths. However, this was not observed in unfocused spindles (**Figure 1K**). In unfocused spindles, the sum of sister k-fiber lengths was indistinguishable from control when averaged over time, but their sum was less conserved over time, yielding higher coefficients of variation (**Figure 1K-N**). Thus, poles help coordinate lengths across sister k-fibers such that chromosomes can move within the metaphase spindle while maintaining spindle length.

Together, our findings indicate that spindle poles are not required to globally maintain k-fiber length. Instead, individual k-fibers can locally maintain their length scale over time, and poles and global pole-focusing forces are needed to coordinate k-fiber lengths within the cell and across sister k-fibers, organizing the spindle's structure in space and time.

Figures

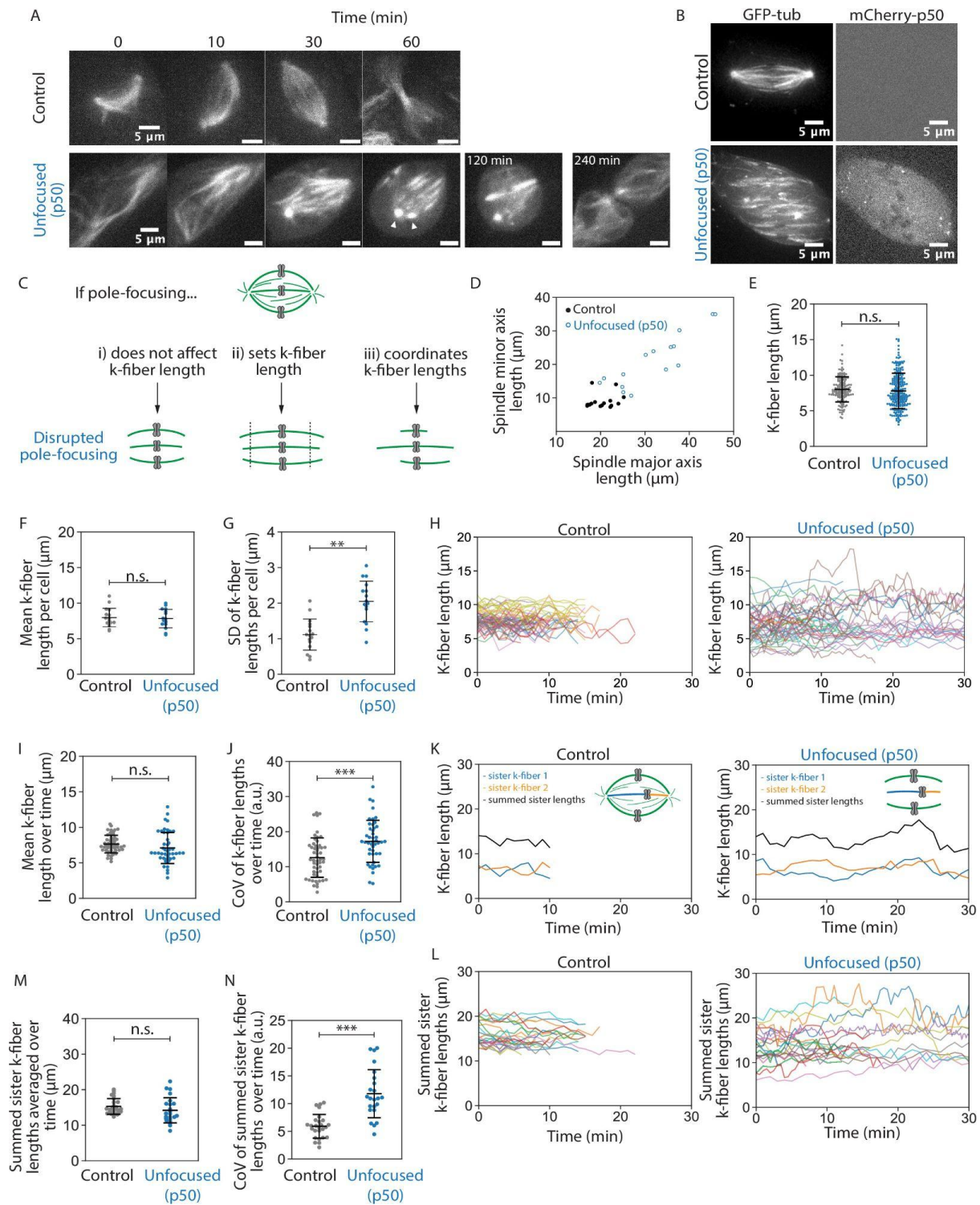


Figure 1. Spindle poles coordinate but do not maintain kinetochore-fiber lengths.
(Figure caption continued on the next page.)

(Figure caption continued from the previous page.)

See also **Videos 1, 2, 3.** **(A)** Representative confocal timelapse images of spindle assembly showing max-intensity z-projections of HaloTag-b-tubulin PtK2 spindles labeled with JF 646, from nuclear envelope breakdown at $t=0$ through cytokinesis. mCherry-p50 was infected into unfocused but not control cells. Arrowheads mark where both centrosomes were observed to be disconnected from the spindle. **(B)** Max-intensity z-projections of representative confocal images of PtK2 spindles with GFP- α -tubulin (control and unfocused) and mCherry-p50 (unfocused only). **(C)** Cartoon model of a mammalian spindle with chromosomes (gray) and microtubules (green), with predictions for k-fiber lengths after disrupting poles. Figures D-G are from the same dataset (Control: $N = 16$ cells; Unfocused: $N = 16$ cells). **(D)** Spindle major and minor axis lengths in control and unfocused spindles. (Major axis Control = $20.24 \pm 2.65 \mu\text{m}$, Unfocused = $31.87 \pm 7.85 \mu\text{m}$, $p = 6.3e-5$; Minor axis: Control = $8.96 \pm 2.12 \mu\text{m}$, Unfocused = $21.23 \pm 7.61 \mu\text{m}$; $p = 2.5e-5$; Control $N = 16$, Unfocused $N = 15$). **(E)** Lengths of control and unfocused k-fibers from z-stacks by live-cell imaging. (Control: $n = 144$ k-fibers, $8.01 \pm 1.76 \mu\text{m}$; Unfocused: $n = 222$ k-fibers, $7.81 \pm 2.52 \mu\text{m}$; $p = 0.38$) **(F)** Mean lengths of control and unfocused k-fibers averaged by cell (Control: $7.97 \pm 1.30 \mu\text{m}$; Unfocused: $7.84 \pm 1.31 \mu\text{m}$; $p = 0.79$). **(G)** Length standard deviation of control and unfocused k-fibers per cell. (Control: $1.12 \pm 0.44 \mu\text{m}$; Unfocused: $2.05 \pm 0.58 \mu\text{m}$; $p = 2.9e-5$) Figures H-N are from the same dataset (Control: $N = 9$ cells, $n = 52$ k-fibers; Unfocused: $N = 9$ cells, $n = 46$ k-fibers). **(H)** Lengths of k-fibers measured over time in control and unfocused spindles. Each trace represents one k-fiber; each color represents a cell. **(I)** K-fiber length averaged over time in control and unfocused spindles. Each point represents one k-fiber. (Control: $7.64 \pm 1.23 \mu\text{m}$; Unfocused: $7.09 \pm 2.19 \mu\text{m}$; $p = 0.14$) **(J)** Coefficients of variation for k-fiber lengths over time in control and unfocused spindles. Each point represents one k-fiber. (Control: 12.60 ± 5.62 a.u.; Unfocused: 17.23 ± 5.98 a.u.; $p = 1.8e-4$). Figures K-N were analyzed by sister k-fiber pairs (Control: $N = 9$ cells, $n = 26$ k-fiber pairs; Unfocused: $N = 9$ cells, $n = 23$ k-fiber pairs) **(K)** Lengths of sister k-fibers were measured over time in control and unfocused spindles. One representative k-fiber for each condition is shown in orange, its sister in blue, and their sum in black. **(L)** The sum of sister k-fiber lengths over time in control and unfocused spindles. Each trace is one sister k-fiber pair. **(M)** Summed sister k-fiber lengths averaged over time (from L). Each dot represents one sister k-fiber pair. (Control: 15.27 ± 2.19 a.u.; Unfocused: 14.18 ± 3.54 a.u.; $p = 0.22$). **(N)** Coefficient of variation of summed sister k-fiber lengths over time (from L). Each dot represents one sister k-fiber pair. (Control: $5.90 \pm 2.14 \mu\text{m}$; Unfocused: $11.77 \pm 4.34 \mu\text{m}$; $p = 2.4e-6$). Numbers are mean \pm standard deviation. Significance values determined by Welch's two-tailed t-test denoted by n.s. for $p \geq 0.05$, * for $p < 0.05$, ** for $p < 0.005$, and *** for $p < 0.0005$.

Supplemental Figures

Video 1. Control spindle assembly in the presence of pole-focusing forces.

In control cells, k-fibers form focused spindles. See also **Figure 1A**. Max intensity projection of live confocal imaging of a PtK2 cell expressing HaloTag-tubulin with JF 646 dye. Time is in hr:min with $t = 0$ at nuclear envelope breakdown. Scale bar, $5\mu\text{m}$.

Video 2. Spindle assembly with inhibited pole-focusing forces.

In p50-overexpressing cells, k-fibers grow to eventually form an unfocused spindle. See also **Figure 1A**. Max intensity projection of live confocal imaging of a PtK2 cell expressing mCherry-p50 and HaloTag-tubulin with JF 646 dye. Time is in hr:min with $t = 0$ at nuclear envelope breakdown. Scale bar, $5\mu\text{m}$.

Video 3. Kinetochores-fiber lengths over time in metaphase: control vs unfocused spindle.

A timelapse of k-fibers in control (left) and unfocused (right) spindles during metaphase. Max intensity projection of live confocal imaging of a PtK2 cell expressing GFP- α -tubulin and mCherry-p50 (unfocused only). Time is in hr:min. Scale bar, $5\mu\text{m}$. Videos were cropped and rotated so k-fibers are latitudinal.

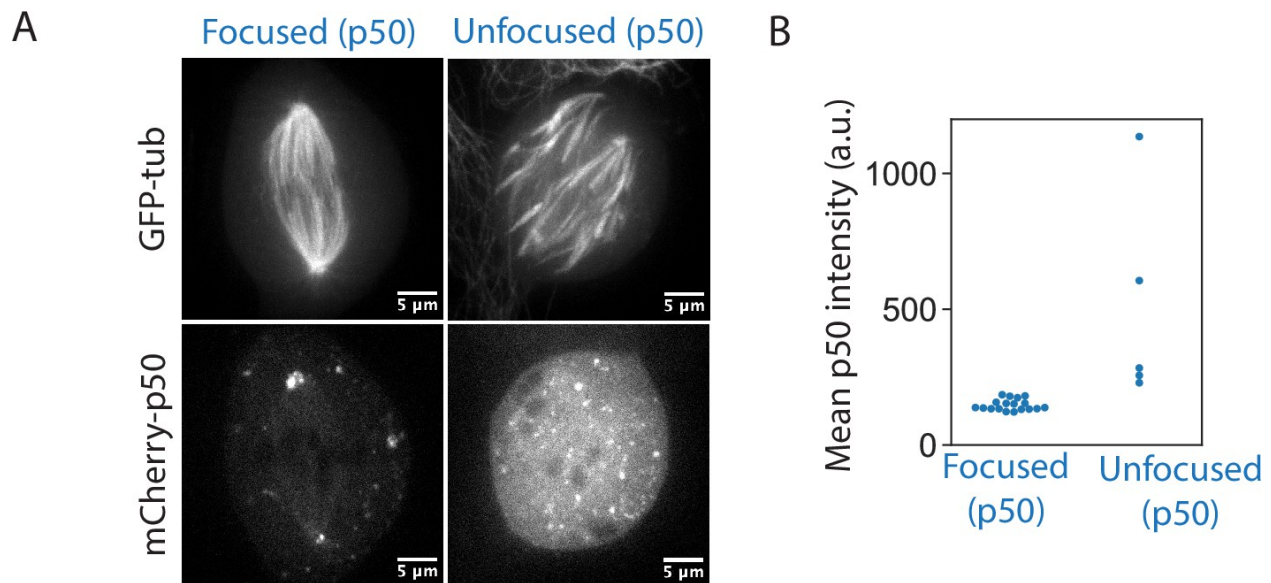


Figure supplement 1. High cytoplasmic p50 intensity correlates with unfocused spindles.

(A) Max-intensity z-projections of confocal images of PtK2 spindles transfected with GFP- α -tubulin and mCherry-p50 representing the two main phenotypes of p50 expression. p50 images show one central z-plane at equal brightness/contrast levels. (Figure caption continued on the next page.)

(Figure caption continued from the previous page.)

(B) Mean p50 intensity per cell was compared between p50-expressing focused spindles and p50-expressing unfocused spindles across one day of imaging. Results were not pooled across multiple days due to laser instability. (Focused p50: n = 18; Unfocused p50: n = 5).

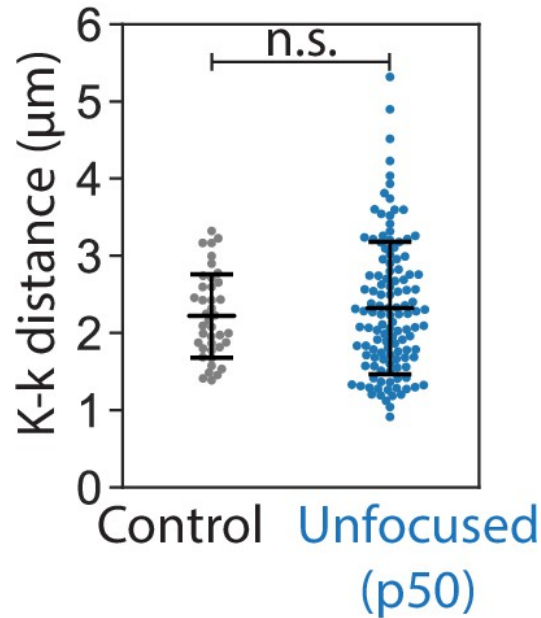


Figure supplement 2. Interkinetochore distance is preserved in unfocused spindles.

Interkinetochore distance between sister k-fibers as measured in confocal live-cell imaging of PtK2 spindles expressing GFP- α -tubulin (control and unfocused) and mCherry-p50 (unfocused only). (Control: N = 13 cells, n = 40 kinetochore pairs, $2.22 \pm 0.54 \mu\text{m}$; Unfocused: N = 16 cells, n = 123 kinetochore pairs, $2.32 \pm 0.86 \mu\text{m}$; p = 0.38). Numbers are mean \pm standard deviation. Significance values determined by Welch's two-tailed t-test denoted by n.s. for $p \geq 0.05$.

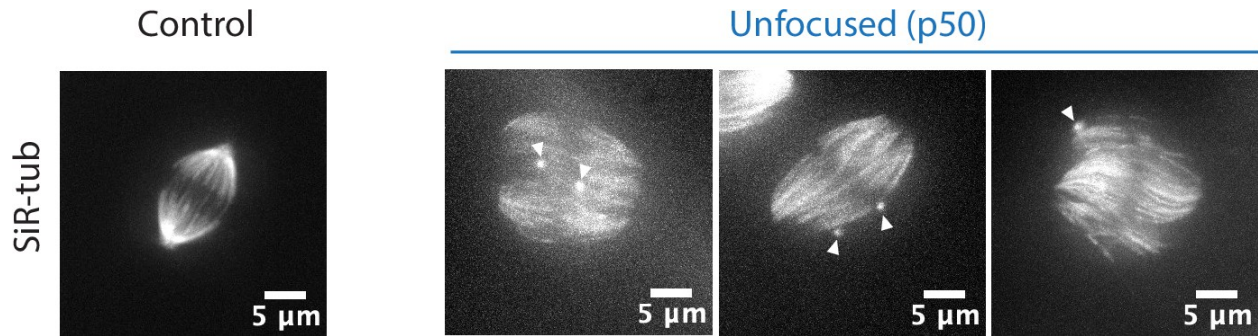


Figure supplement 3. p50 overexpression in RPE1 cells generates unfocused spindles.

Representative confocal images showing max-intensity z-projections of RPE1 metaphase spindles labeled with SiR-tubulin. mCherry-p50 was expressed in unfocused but not control cells. Arrowheads mark centrosomes that appeared disconnected from spindles.

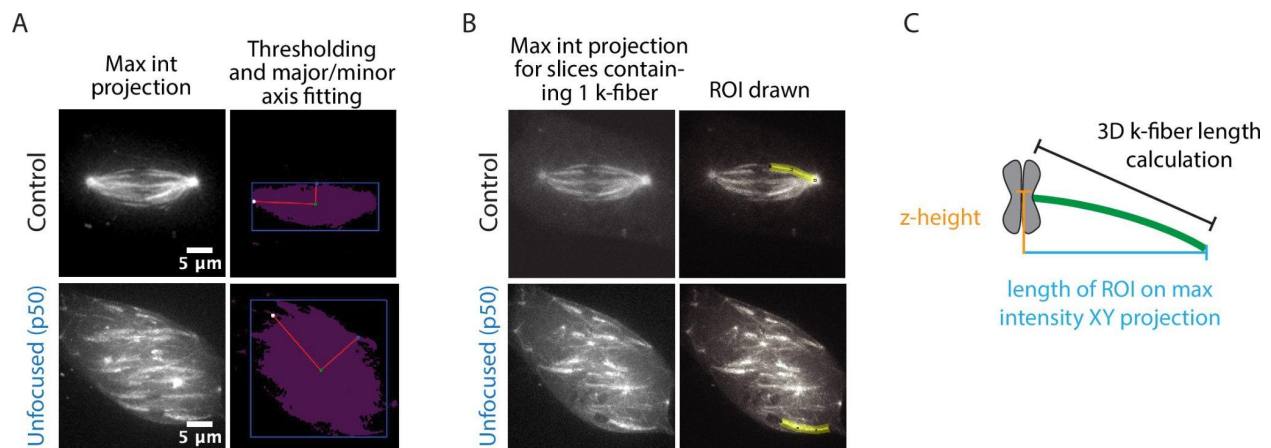


Figure supplement 4. Length measurement methods.

(A) Spindle major and minor axis length measurement. Example maximum intensity projection images of control and unfocused spindles from **Figure 1B** (left). Images were rotated, cropped, thresholded using the Otsu filter, and fitted with ellipses with major and minor axes calculated using SciKit's region property measurements (right). **(B)** Individual k-fiber length measurement. Example maximum intensity projections of control and unfocused spindles in A including only the subset of z-slices where the k-fiber of interest was in focus (left). An example ROI drawn in FIJI is shown to the right. **(C)** Cartoon depicting 3D length calculation. Lengths of ROIs as drawn in B were measured to calculate the XY length of k-fibers (blue). Z-height of k-fibers was calculated based on the number of z-slices the k-fiber spanned and the size of the z-step (orange). The Pythagorean theorem was used to approximate the 3D length of k-fibers in XYZ (black). In focused control k-fibers, centrosome radius was then subtracted (as calculated in **Figure supplement 5**).

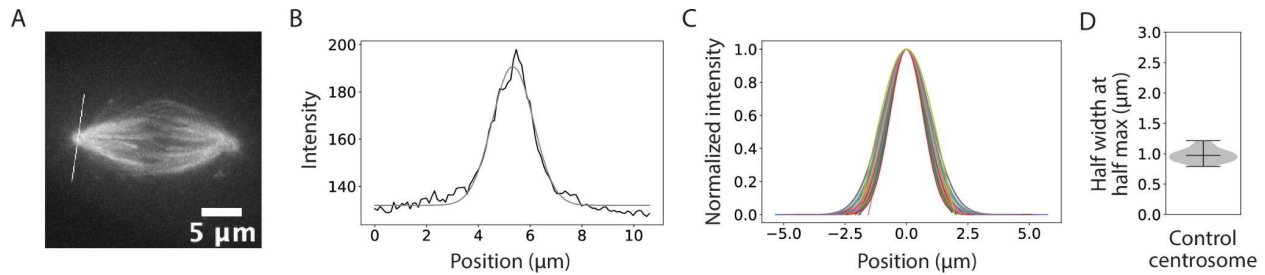


Figure supplement 5. Centrosome radius approximation.

(A) Example line ROI drawn on a representative centrosome in a max-intensity z-projection of a confocal image of a PtK2 spindle expressing GFP- α -tubulin. **(B)** Line profile of the example centrosome in A. Raw intensity values along the line ROI are plotted in black. These data were smoothed by applying a Gaussian fit and plotted in gray. **(C)** Normalized Gaussian-fitted line profiles of centrosomes. Each color refers to one Gaussian-fitted and normalized centrosome line profile. Traces were normalized by max intensity. **(D)** Centrosome radius was approximated by calculating the half width at half maximum from traces in C. (N = 16 cells, n = 32 centrosomes, $0.97 \pm 0.10 \mu\text{m}$). Numbers are mean \pm standard deviation.

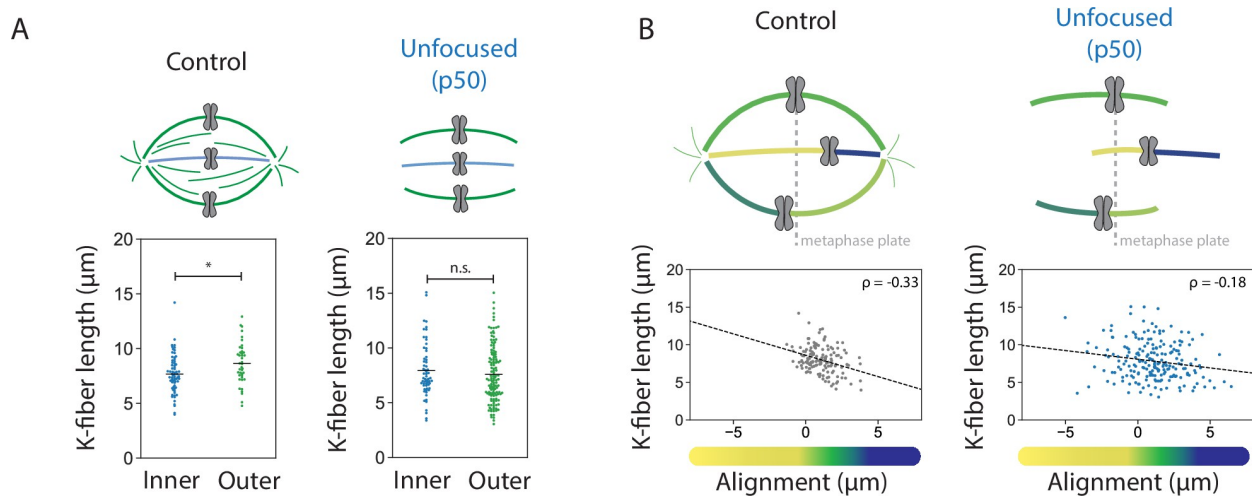


Figure supplement 6. Kinetochores-fiber lengths are spatially correlated in control but not unfocused spindles.

(A) Comparison of innermost and outermost k-fiber lengths in control and unfocused spindles. Inner k-fibers were defined to be within $2 \mu\text{m}$ of the long spindle axis; outer k-fibers were 3 or more μm away. (Control: N = 16 cells, inner n k-fibers = 68, inner mean length = $7.67 \pm 1.72 \mu\text{m}$, outer n k-fibers = 41, outer mean length $8.64 \pm 1.86 \mu\text{m}$, $p = 0.0070$; Unfocused: N = 16 cells, inner n k-fibers = 61, inner mean length = $7.92 \pm 2.46 \mu\text{m}$, outer n k-fibers = 131, outer mean length $7.59 \pm 2.57 \mu\text{m}$, $p = 0.40$). **(B)** Correlation of k-fiber length and kinetochore alignment along the metaphase plate in control and unfocused spindles. Alignment was measured based on kinetochore (Figure caption continued on the next page.)

(Figure caption continued from the previous page.)
distance to the approximated metaphase plate line and direction of misalignment. More negative values correspond to over-aligned kinetochores whose attached k-fibers are expected to be longer (yellow). More positive values correspond to under-aligned kinetochores (blue). Alignment scores around 1 μm correspond to kinetochore pairs aligned at the metaphase plate (green). Line of best fit is shown. (Control: N = 16 cells, n = 139 k-fibers, correlation coefficient $\rho = -0.33$; Unfocused: N = 16 cells, n = 205 k-fibers, correlation coefficient $\rho = -0.18$). Numbers are mean \pm standard deviation. Significance values determined by Welch's two-tailed t-test denoted by n.s. for $p \geq 0.05$ and * for $p < 0.05$. Pearson's correlation coefficients are reported.

Chapter 2. Dynamics and length regulation in kinetochore-fibers

Introduction

We have shown that k-fibers can establish and maintain their length independently of poles and pole-focusing forces, but cannot properly organize their lengths within the spindle across space and time. While unfocused k-fibers within a cell maintain their average length over time, we sought to determine whether they can recover their length without focused poles, that is, whether they actively adjust and recover their length if shortened below their steady-state length.

Results

Kinetochore-fibers recover their lengths without focused poles

First, we used laser ablation to acutely cut and shorten k-fibers and then imaged their regrowth compared to unablated k-fibers (**Figure 2A-D, Video 4**). Mean k-fiber lengths in unfocused spindles before ablation appeared to be shorter (**Figure 2D**); however, this was due to not capturing the full length of k-fibers in a single z-plane while imaging ablated k-fibers. Indeed, length analysis of full z-stacks from unfocused spindles before ablation yielded an indistinguishable mean k-fiber length compared to control k-fibers in **Figure 1E (Figure supplement 7)**. Thus, ablated k-fibers were compared to their unablated neighbors as internal controls. Ablation generates new microtubule minus-ends on the shortened k-fiber stub, which recruit NuMA and dynein to reincorporate them back into the pole in control cells (Elting et al., 2014; Sikirzhyski et al., 2014). As expected, control ablated k-fibers were transported towards poles and

did so while growing back rapidly following ablation, at $0.85 \pm 0.09 \mu\text{m}/\text{min}$ on average in the first 5 minutes (**Figure 2E**). Unfocused k-fibers also grew back, though more slowly at $0.38 \pm 0.42 \mu\text{m}/\text{min}$ on average (**Figure 2E**). They took longer to grow back to the mean length of unablated neighbor k-fibers neighbor k-fibers (**Figure 2F**). Thus, focused poles and pole-focusing forces are not required for k-fibers to recover their lengths, but are required for rapid length recovery. The latter is consistent with the idea that force on k-fiber ends favors k-fiber growth (Dumont and Mitchison, 2009a; Long et al., 2020; Nicklas and Staehly, 1967). Ultimately, k-fibers can adapt to length changes and maintain a steady-state length locally, without poles.

To test whether neighboring k-fibers or existing microtubule networks provide information for length maintenance, we treated spindles with nocodazole to depolymerize all microtubules, then washed it out and imaged spindle reassembly (**Figure 2G, Video 5**). After 10 minutes, control spindle k-fibers had regrown to within 1 μm of their original length, albeit shorter on average, and unfocused spindle k-fibers fully recovered their average length and grew back into an unfocused state (**Figure 2G-I, Video 5**). Both control and unfocused spindles could enter anaphase after nocodazole washout (**Figure 2G, Video 5**). Thus, cells lacking pole-focusing forces in metaphase can self-assemble unfocused spindles with k-fibers of about the same length as control k-fibers. This supports a model of k-fibers regulating their own lengths without cues from pre-existing microtubule networks or neighboring k-fibers to build a bi-oriented spindle of the correct length scale.

Kinetochores-fibers exhibit reduced end dynamics in the absence of poles and pole-focusing forces

Given that k-fibers can maintain (**Figure 1**) and recover (**Figure 2**) their mean length without poles and pole focusing-forces—albeit regrowing more slowly—we asked whether unfocused k-fibers are dynamic and whether they have reduced dynamics. If dynamics are locally set for each individual k-fiber, dynamics should not change without poles or pole-focusing forces; if dynamics are set by global pole-focusing forces, we expect different dynamics without poles. In principle, dynamics can be probed using autocorrelation analysis, which reveals the timescale over which k-fibers “remember” their length. If k-fibers were less dynamic and their lengths changed more slowly, this would result in stronger autocorrelation and autocorrelation for a longer period. Indeed, this is what we observed in unfocused k-fibers compared to control, consistent with unfocused k-fibers having reduced dynamics (**Figure 3A**). We thus sought to directly measure k-fiber end dynamics and flux.

At metaphase, k-fiber ends are dynamic, with poleward flux associating with net polymerization at plus-ends and apparent depolymerization at minus-ends (Mitchison, 1989). Spindle poles have been proposed to regulate minus-end dynamics (Dumont and Mitchison, 2009a; Gaetz and Kapoor, 2004; Ganem and Compton, 2004). To measure k-fiber dynamics, we introduced a bleach mark on a k-fiber and tracked its position over time relative to k-fiber minus-ends (**Figure 3B-D, Video 6**). In control spindles, the mark approached minus-ends at a rate of $0.55 \pm 0.29 \mu\text{m}/\text{min}$, consistent with previous reports (**Figure 3D, Figure 4D**, Cameron et al., 2006; Mitchison, 1989). In unfocused spindles, the mark approached minus-ends much slower at a rate of $0.13 \pm$

0.15 $\mu\text{m}/\text{min}$ (**Figure 3D, Figure 4D**). These findings are in contrast to work in *Xenopus* showing that dynein inhibition through p50 overexpression does not impact the flux rate in the central spindle (Yang et al., 2008), but are supported by work in *Xenopus* and in mammals showing that dynein contributes to poleward transport (Burbank et al., 2007; Lecland and Lüders, 2014; Steblyanko et al., 2020). Thus, spindle poles or pole-focusing forces are required for fast k-fiber end dynamics, likely contributing to less efficient k-fiber length maintenance in unfocused spindles.

Kinetochores tune their end dynamics to recover length, without pole-focusing forces

The fact that unfocused k-fibers grow back to a steady-state length after being acutely shortened (**Figure 2**) suggests that they can tune their dynamics after shortening. We thus sought to determine the physical mechanism for length recovery (**Figure 4A**). One model is that minus-end depolymerization stops or slows—for example, pole-based depolymerization dynamics are lost while k-fiber minus-ends appear separated from the pole (Dumont and Mitchison, 2009a; Long et al., 2020). Another model is that plus-end polymerization increases, which could occur in either a force-dependent manner (Akiyoshi et al., 2010; Dumont and Mitchison, 2009a; Long et al., 2020; Nicklas and Staehly, 1967) or a length-dependent manner (Dudka et al., 2019; Mayr et al., 2007; Stumpff et al., 2008; Varga et al., 2006). Notably, we find that k-fibers can grow back after ablation (**Figure 2E**) at a rate faster than poleward flux and associated minus-end dynamics in both control and unfocused spindles ($0.85 \pm 0.09 \mu\text{m}/\text{min}$ vs $0.55 \pm 0.29 \mu\text{m}/\text{min}$ in control, $0.38 \pm 0.42 \mu\text{m}/\text{min}$ vs $0.13 \pm 0.15 \mu\text{m}/\text{min}$ in unfocused) (**Figure 2E, Figure 4D**). Thus, even if minus-end dynamics were

suppressed, this would not be sufficient to account for the k-fiber regrowth we observe after ablation, with or without pole-focusing forces.

To directly test how changes in k-fiber length regulate end dynamics, and if this mechanism depends on pole-focusing forces, we ablated a k-fiber and introduced a photobleach mark on it in control and unfocused spindles (**Figure 4A, B, Video 7**). In control spindles, the photomark did not detectably approach the minus-end of the k-fiber during its regrowth (**Figure 4B, C**), indicating that suppression of minus-end dynamics contributes to k-fiber regrowth, as in *Drosophila* cells (Maiato et al., 2004; Matos et al., 2009). Consistent with k-fiber minus-end dynamics being transiently suppressed during regrowth, rather than frozen due to ablation damage, k-fiber minus-ends resumed depolymerization in control spindles after ablation and length recovery (**Figure supplement 8, Video 8**). However, while *Drosophila* k-fibers regrow at the rate of poleward flux, these control mammalian k-fibers regrew faster than the rate of flux, indicating that mammalian k-fibers must additionally increase their plus-end dynamics when shortened to reestablish their steady-state length. In unfocused spindles, the photomark also did not detectably approach the minus-end of the k-fiber during its regrowth (**Figure 4C**), consistent with suppression of any minus-end dynamics, though it was not significantly different from the already slow dynamics and insufficient to account for growth (**Figure 4D**). Thus, k-fibers can tune their plus-end dynamics to recover their length in the absence of dynein-based pole-focusing forces. This supports a model where k-fiber length is not simply regulated by global pole-focusing forces, but by local length-based mechanisms.

Figures

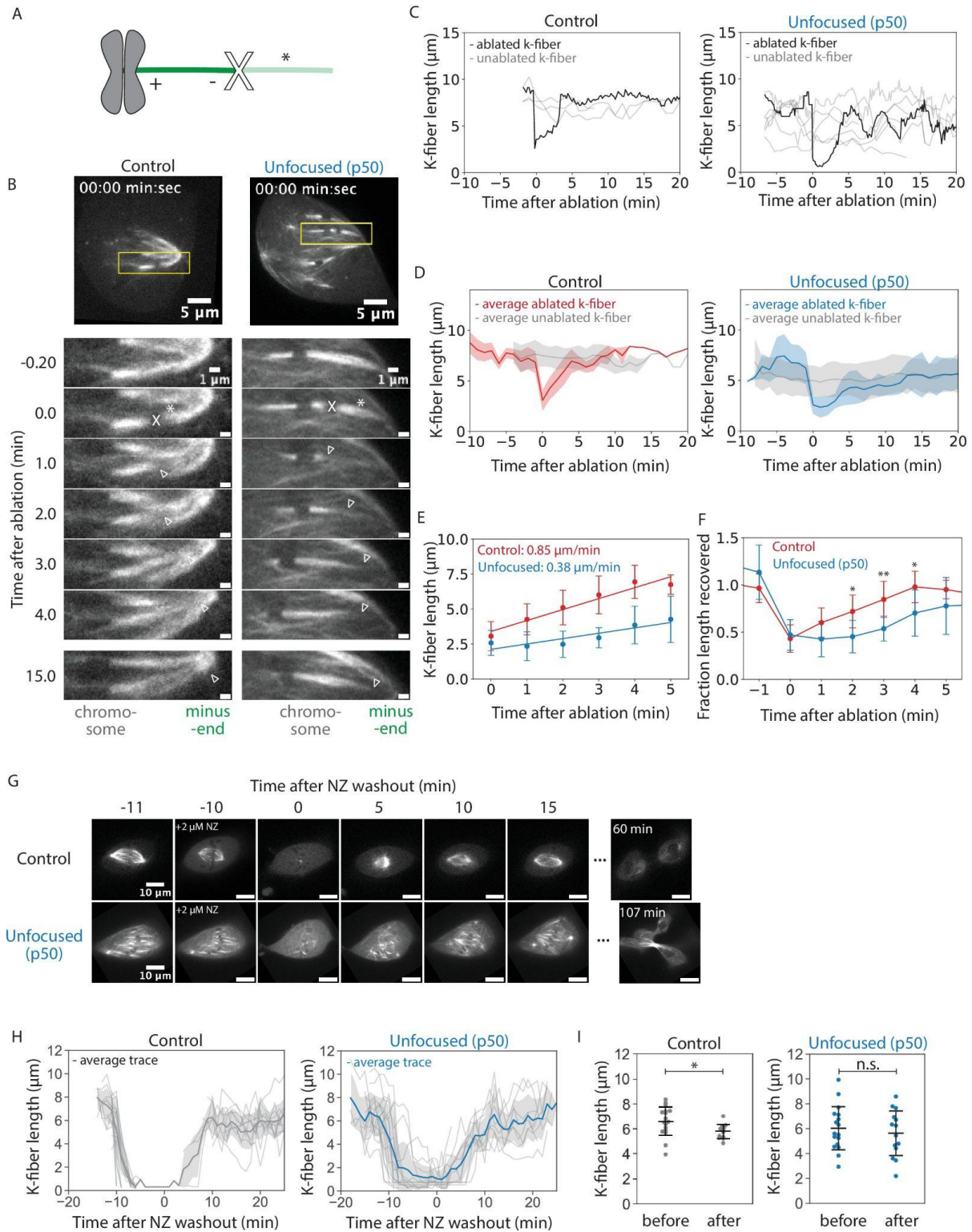


Figure 2. Kinetochores recover their lengths without focused poles.
 See also Videos 4,5.
 (Figure caption continued on the next page.)

(Figure caption continued from the previous page.)

(A) Schematic of a k-fiber after ablation at position X. The k-fiber stub still attached to the chromosome persists with a new minus-end (dark green). The k-fiber segment closer to the pole with a new plus-end depolymerizes away (light green, *). **(B)** Representative confocal timelapse images of PtK2 k-fibers with GFP- α -tubulin and mCherry-p50 (in unfocused only). K-fibers were laser-ablated at $t = 0$ (X) and followed over time. Empty arrowheads mark newly created minus-ends. **(C)** K-fiber lengths over time in a representative control and unfocused spindle. Gray traces represent unablated k-fibers. The ablated k-fiber is plotted in black. **(D)** Binned and averaged k-fiber lengths over time for ablated control and unfocused spindles. The average length of non-ablated k-fibers is plotted in gray, the average of ablated k-fibers in red for control and blue for unfocused. Shaded colors indicate ± 1 standard deviation for their respective condition. (Control: $N = 7$ cells, $n = 8$ ablated k-fibers, $m = 26$ non-ablated k-fibers; Unfocused: $N = 6$ cells, $n = 8$ ablated k-fibers, $m = 31$ non-ablated k-fibers). **(E)** Average growth rates of k-fibers immediately following ablation. Linear regression was performed on binned k-fiber lengths during the first five minutes following ablation (Control: $0.85 \pm 0.09 \mu\text{m}/\text{min}$, Unfocused: $0.38 \pm 0.42 \mu\text{m}/\text{min}$, $p = 0.023$). **(F)** Fraction of length recovered following ablation relative to the mean of unablated k-fibers in control and unfocused k-fibers. The average trace for unablated k-fibers in D was averaged over time and ablated lengths were normalized to this value. Times with statistically significant differences in length recovery are denoted by *. **(G)** Representative confocal timelapse images of PtK2 spindles with GFP- α -tubulin (in control and unfocused) and mCherry-p50 (in unfocused only), with $2 \mu\text{M}$ nocodazole added at -10 min and washed out at $t = 0$. **(H)** Lengths of k-fibers over time during nocodazole washout. All k-fibers are shown with the average trace plotted with ± 1 standard deviation shaded in light gray. (Control: $N = 3$ cells, $n = 28$ k-fibers; Unfocused: $N = 4$ cells, $n = 23$ k-fibers). **(I)** Mean k-fiber lengths before nocodazole and after washout in control and unfocused spindles. (Control before: $6.58 \pm 1.15 \mu\text{m}$, $n = 17$; Control after: $5.76 \pm 0.57 \mu\text{m}$, $n = 12$, $p = 0.02$; Unfocused before: $6.03 \pm 1.73 \mu\text{m}$, $n = 17$; Unfocused after: $5.63 \pm 1.80 \mu\text{m}$, $n = 14$, $p = 0.55$) Numbers are mean \pm standard deviation. Significance values determined by Welch's two-tailed t-test denoted by * for $p < 0.05$, ** for $p < 0.005$, and *** for $p < 0.0005$.

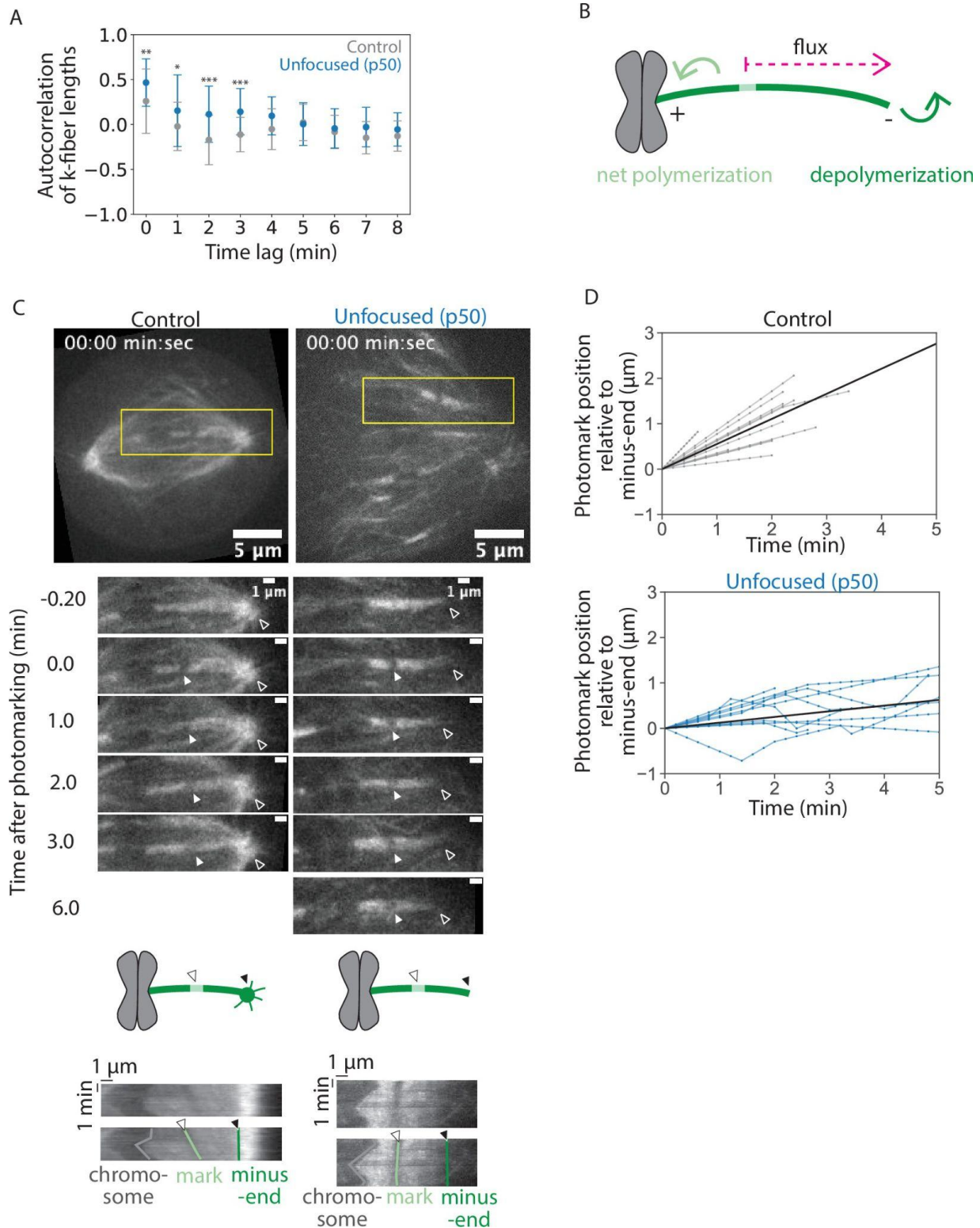


Figure 3. Kinetochore-fibers exhibit reduced end dynamics in the absence of poles and pole-focusing forces.

(Figure caption continued on the next page.)

(Figure caption continued from the previous page.)

See also **Video 6**. **(A)** Autocorrelation of k-fiber lengths over time from **Figure 1H** for control and unfocused k-fibers. Calculations and statistical analysis were performed using built-in Mathematica functions, where * indicates $p < 0.05$. **(B)** Schematic of a photomark (light green) on a k-fiber (dark green). The dotted arrow shows the direction the photomark moves with flux in control, where displacement of the mark towards the minus-end increases over time. Net end dynamics are shown by curved arrows (equal at steady-state). **(C)** Representative confocal timelapse images of PtK2 k-fibers with GFP- α -tubulin (in control and unfocused) and mCherry-p50 (in unfocused only). A bleach mark was made at time = 0 and followed over time (filled arrowhead). Empty arrowheads indicate minus ends. Below: Kymographs of the above images. Each row of pixels represents a max intensity projection of a 5-pixel high stationary box drawn around the k-fiber at one time point (yellow box). **(D)** Minus-end dynamics, where photomark position over time describes how the mark approaches the k-fiber's minus-end over time in control and unfocused k-fibers. Each trace represents one mark on one k-fiber. To measure flux as defined by minus-end depolymerization, the movement of the photomark towards the minus-end was plotted over time. Line with the average slope is drawn in black. (Control: N = 8 cells, n = 12 k-fibers; Unfocused: N = 8 cells, n = 11 k-fibers). Numbers are mean \pm standard deviation. Significance values determined by Welch's two-tailed t-test denoted by n.s. for $p \geq 0.05$, * for $p < 0.05$, ** for $p < 0.005$, and *** for $p < 0.0005$.

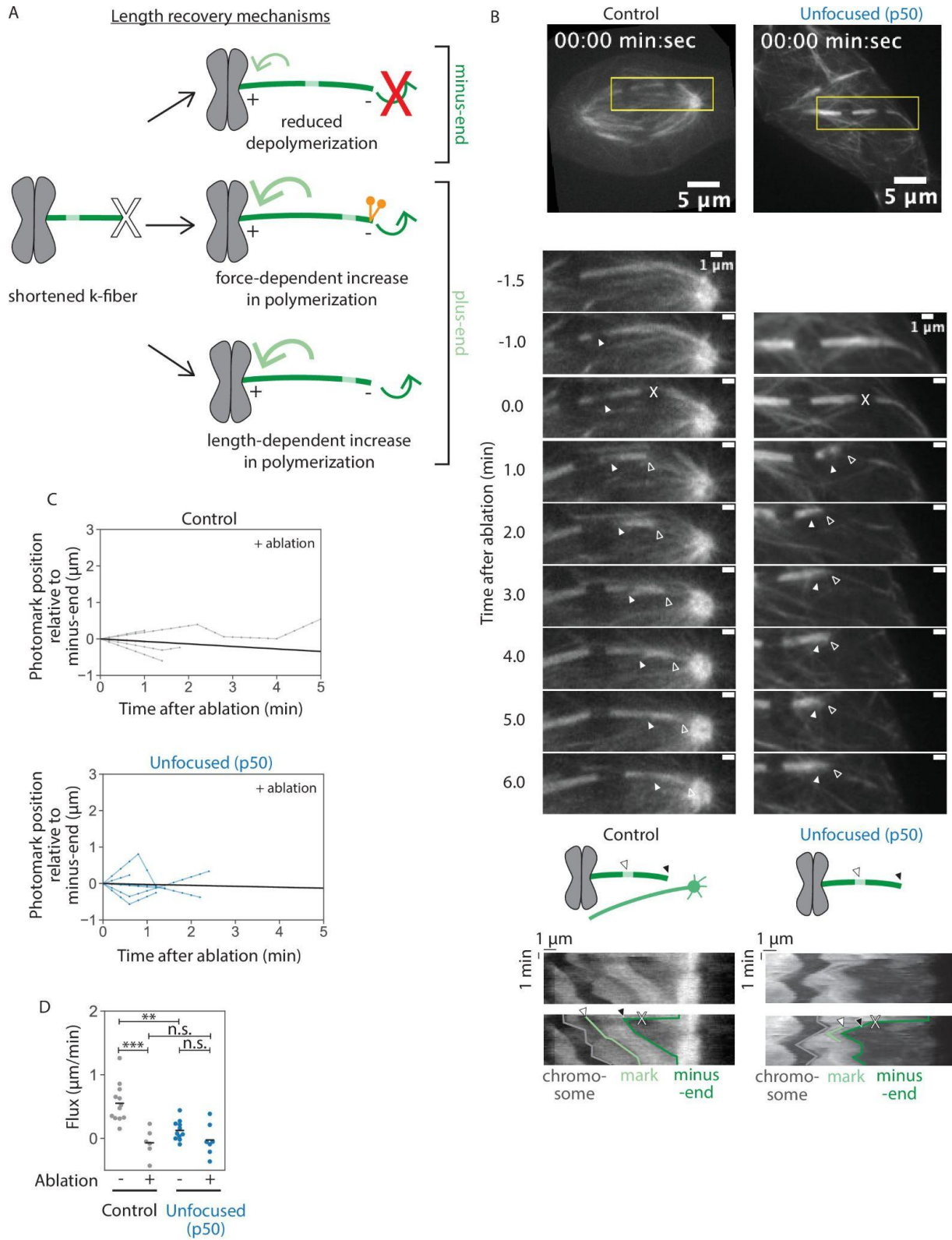


Figure 4. Kinetochore-fibers tune their end dynamics to recover length, without pole-focusing forces.

(Figure caption continued on the next page.)

(Figure caption continued from the previous page.)

See also **Video 7**. **(A)** Models describing k-fiber length recovery mechanisms. K-fibers shortened by ablation (X) with a photomark (light green) can potentially grow back in different ways: suppression of minus-end depolymerization (top), increased plus-end polymerization induced by forces such as dynein (middle), or increased polymerization in a length-dependent manner (bottom). **(B)** Representative confocal timelapse images of PtK2 k-fibers with GFP- α -tubulin (in control and unfocused) and mCherry-p50 (in unfocused only). Filled arrowhead follows a bleach mark. At $t = 0$, k-fibers were cut with a pulsed laser at higher power (X). Empty arrowhead follows the new k-fiber minus-end. Below: Kymographs of the above images as prepared in **Figure 3C**. **(C)** Minus-end dynamics were probed by tracking movement of the mark towards the k-fiber's minus-end over time in control and unfocused k-fibers after ablation at $t = 0$. Line with the average slope is drawn in black. (Control: $N = 5$ cells, $n = 6$ k-fibers; Unfocused: $N = 7$ cells, $n = 7$ k-fibers). **(D)** Minus-end dynamics of k-fibers. Flux as measured by rate of photomark movement towards the minus-end with or without ablation in control and unfocused k-fibers. Each point represents the slope of one trace in **Figure 3D** or **Figure 4C** measured by linear regression (Control: mean flux = $0.55 \pm 0.29 \mu\text{m}/\text{min}$, mean flux after ablation = $-0.07 \pm 0.20 \mu\text{m}/\text{min}$; Unfocused: mean flux = $0.13 \pm 0.15 \mu\text{m}/\text{min}$, mean flux after ablation = $-0.03 \pm 0.23 \mu\text{m}/\text{min}$; p non-ablated control vs. ablated control = $2.7\text{e-}4$, p non-ablated control vs. non-ablated unfocused = $5.3\text{e-}4$, p non-ablated unfocused vs. ablated unfocused = 0.19 , p ablated control vs. ablated unfocused = 0.75). Numbers are mean \pm standard deviation. Significance values determined by Welch's two-tailed t-test denoted by n.s. for $p \geq 0.05$, * for $p < 0.05$, ** for $p < 0.005$, and *** for $p < 0.0005$.

Supplemental Figures

Video 4. Ablating kinetochore-fibers: control vs unfocused spindle.

Control (left) and unfocused (right) k-fibers grow back after being severed by a laser. See also **Figure 2B**. Live confocal imaging of a PtK2 cell expressing GFP- α -tubulin and mCherry-p50 (unfocused only). The ablation site is marked by 'X', causing the segment containing the old minus-end of the k-fiber to quickly depolymerize (*). The new stable minus-end is tracked by the empty arrowhead. Time is in min:sec, with ablation occurring at $t = 0$. Scale bar, $5\mu\text{m}$.

Video 5. Spindle assembly after nocodazole washout: control vs unfocused spindle.

Control (left) and unfocused (right) spindles grow back robustly after washing out nocodazole, a microtubule-destabilizing drug. See also **Figure 2G**. Live confocal imaging of a PtK2 cell expressing GFP- α -tubulin and mCherry-p50 (unfocused only). $2 \mu\text{M}$ nocodazole was added for 10 min before 10 washes in warmed media were started at $t = 0$. Time is in hr:min. Scale bar, $5\mu\text{m}$.

Video 6. Photobleaching kinetochore-fibers to measure microtubule flux: control vs unfocused spindle.

Control (left) and unfocused (right) k-fibers exhibit poleward flux (reduced in unfocused spindles) as demonstrated by a bleach mark on a k-fiber moving towards a pole over time. See also **Figure 3C**. Live confocal imaging of a PtK2 cell expressing GFP- α -tubulin and mCherry-p50 (unfocused only). The laser-induced bleach mark is tracked by the filled arrowhead over time as its associated tubulin moves away from the kinetochore towards the minus-end (empty arrowhead). Time is in min:sec, with the photomark created at $t = 0$. Scale bar, 5 μ m.

Video 7. Ablating and photomarking kinetochore-fibers: control vs unfocused spindle.

Control (left) and unfocused (right) k-fibers exhibit no measurable minus-end depolymerization during regrowth after ablation. See also **Figure 4B**. Live confocal imaging of a PtK2 cell expressing GFP- α -tubulin and mCherry-p50 (unfocused only). The ablation site is marked by 'X' and the new stable minus-end is tracked by the empty arrowhead. The photomark is tracked by the filled arrowhead and it does not appear to get closer to the other arrowhead at the minus-end over time. Time is in min:sec, with ablation occurring at $t = 0$. Scale bar, 5 μ m.

Video 8. Photobleaching control kinetochore-fibers after ablation and length recovery.

Control k-fibers resume minus-end depolymerization after ablation and length recovery. See also **Figure supplement 8**. Live confocal imaging of a PtK2 cell expressing GFP- α -tubulin. The ablation site is marked by 'X' and the new stable minus-end is tracked by the empty arrowhead. The photomark is made several minutes after ablation when k-fiber repair and length recovery are complete. The mark is tracked by the filled arrowhead as it approaches the other arrowhead at the minus-end over time. Time is in min:sec, with ablation occurring at $t = 0$. Scale bar, 5 μ m.

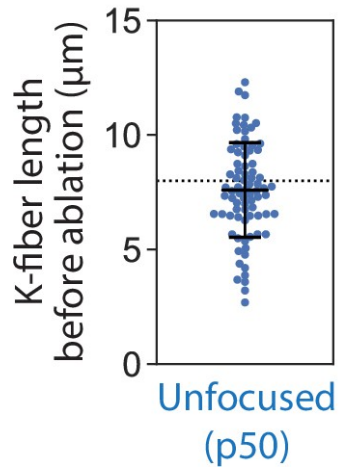


Figure supplement 7. Kinetochores-fiber lengths before ablation.

Lengths of k-fibers in unfocused cells prior to ablation. Lengths were measured in 3D from z-stacks of PtK2 cells expressing GFP- α -tubulin and mCherry-p50 taken by confocal live-imaging, as in **Figure 1E**. The dotted line represents the mean control k-fiber length as calculated in **Figure 1E**. (N = 4 cells, n = 79 k-fibers, $7.60 \pm 2.07 \mu\text{m}$).

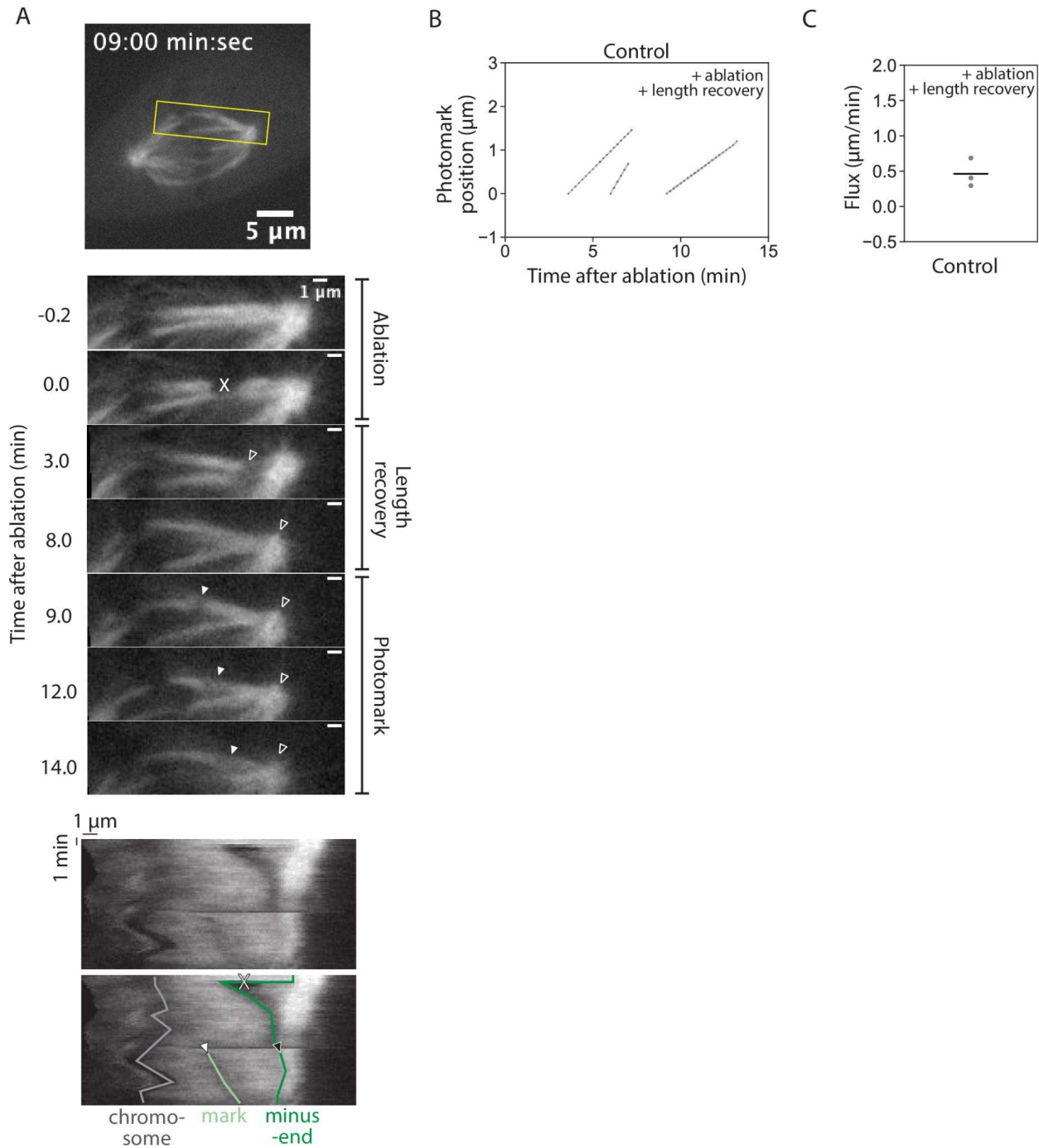


Figure supplement 8. Minus-end depolymerization resumes after length recovery following ablation.

See also **Video 8**. **(A)** Representative confocal timelapse images of PtK2 k-fibers with GFP- α -tubulin. At $t = 0$, k-fibers were cut with a pulsed laser at a high power (X). Empty arrowhead follows the new k-fiber minus-end. Filled arrowhead follows a bleach (Figure caption continued on the next page.)

(Figure caption continued from the previous page.)
mark made several minutes later with the laser at a lower power. Below: Kymographs of the above images as prepared in **Figure 3C**. **(B)** Minus-end dynamics were probed by tracking movement of the mark relative to the k-fiber's minus-end over time in control k-fibers several minutes after ablation ($t = 0$) once k-fiber repair and length recovery were complete. **(C)** Minus-end dynamics of k-fibers. Flux as measured by rate of photomark movement towards the minus-end after ablation and length recovery in control k-fibers. Each point represents the slope of one trace in **Figure supplement 8B** measured by linear regression ($n = 3$ cells, mean = 0.46 ± 0.16 $\mu\text{m}/\text{min}$).

Chapter 3. Probing kinetochore-fiber anchorage

Introduction

Kinetochore-fibers are not only dynamic structures that can regulate their length, they are also capable of producing and responding to a variety of forces in the spindle to position and coordinate them accurately. Within the spindle, motor proteins generate force that extend and contract the spindle (Blangy et al., 1995; Kapitein et al., 2005; Roostalu et al., 2018; Foster et al., 2015; Gaglio et al., 1997; Hueschen et al., 2017; Neahring et al. 2021), k-fiber dynamics generate force to push and pull on chromosomes (Grishchuk et al., 2006; Koshland et al., 1988), and crosslinkers provide local reinforcement between the variety of microtubules within the spindle (Peterman and Scholey 2009). In particular, k-fibers are known to interact with a dense network of non-kinetochore microtubules, crosslinkers, and motor proteins (Steblyanko et al., 2020; Mastronarde et al., 1993; McDonald et al., 1992, Elting et al., 2017; Kajtez et al., 2016; Vladimirov et al., 2013). While kinetochore microtubules turn over on the minutes timescale, non-kinetochore microtubules turn over on the seconds timescale (Gorbsky and Borisy 1989, Saxton et al. 1984, Zhai et al. 1995). Outside the spindle, forces from astral microtubules and cytoplasmic flows are known to position the spindle during cell division (Grill and Hyman 2005, Xie et al. 2022). Thus, the spindle is a structure that remodels in response to forces, yet it needs to be stable enough to maintain its shape throughout mitosis and coordinate its k-fibers to properly segregate chromosomes. How does the spindle robustly withstand and remodel in response to forces?

One major contributor to the spindle's response to force is its viscoelasticity. Viscoelasticity is a material property where both the magnitude and temporality of an applied force affects the material's response. In the regime where elastic forces dominate, deformations are reversible - imagine quickly pulling on a rubber band and watching it immediately snap back into shape as you let go. In the regime where viscous forces dominate, deformations and recovery from deformations happen more slowly - imagine pushing your hand into memory foam and watching it slowly recover when you remove your hand. However, at high enough force, most viscoelastic biological materials can enter a plastic regime, where the deformations become permanent as the material irreversibly remodels.

Several factors are known to influence the material properties of spindles, but how individual spindle components are organized and anchored in this environment is not well understood. It has been shown that metaphase spindles in *Xenopus* exhibit viscoelasticity, where elastic responses dominate when force is applied at short timescales (<10 s), viscous responses dominate when force is applied on intermediate timescales (10-100 s), as well as plastic responses after larger deformations (Itabashi et al. 2009, Shimamoto et al. 2011). Global spindle viscoelasticity is known to depend on dynamic crosslinkers, non-kinetochore microtubules, and dynein-mediated spindle pole organization (Shimamoto et al. 2011). However, *Xenopus* spindles have different architecture than mammalian spindles, consisting of shorter tiled microtubule arrays, whereas mammalian spindles have discrete bundles of microtubules whose microtubules span most of the distance between the chromosomes and the pole (Brugues et al. 2012; McDonald et al., 1992; Kiewisz et al., 2022). Thus, the material

properties of the spindle and mechanisms of k-fiber organization in the mammalian spindle may differ. Here, we disentangle the role of poles and pole-focusing forces from other forces acting on k-fibers to probe their organization and mechanics in the metaphase mammalian spindle.

Preliminary Results

Kinetochores recover displacement from force applied at short timescales regardless of poles

Here, we probe the relaxation of displaced k-fibers using microneedle manipulation to pull on and release k-fibers in the presence or absence of spindle poles (Suresh et al. 2020, Richter et al. 2023). We followed the region of the k-fiber closest to the needle or directly in contact with it to track k-fiber displacement and relaxation. Following a 30 second needle pull of 8 μm and immediate release (**Figure 5A**), the manipulated regions of k-fibers relaxed, though total displacement did not return to 0, indicating some permanent displacement of the k-fiber (**Figure 5B,C**). Some of the permanent displacement is likely attributed to spindle translation and global spindle remodeling. Registering stacks may correct for spindle translation (data not shown), but it is difficult to use this method reliably without introducing artifacts from global spindle and k-fiber remodeling, especially in unfocused spindles. Overall, we conclude that spindles exhibit some relaxation consistent with a viscoelastic response on this timescale.

Since previous work has shown that spindle poles and dynein contribute to elasticity in *Xenopus* spindles (Shimamoto et al. 2011), we directly tested their

contribution to k-fiber force responses by pulling on unfocused k-fibers in p50-overexpressing spindles lacking poles. Unfocused k-fibers were also observed to both relax and display residual displacement on a short timescale (**Figure 5D,E**). Thus, forces affecting k-fiber position on the timescale of ~30 seconds are still active in spindles lacking poles and pole-focusing activity.

Unfocused kinetochore-fibers exhibit permanent displacement at long timescales of force applied compared to control

Next, we tested the response of k-fibers to forces applied on longer timescales, pulling 8 μm for 30 seconds, holding the needle in place for 2 minutes, then releasing. Given that the lifetime of non-kMTs is on the order of 30 seconds (Saxton et al., 1984; Zhai et al., 1995), this hold time should be sufficient to turn over the majority of the non-kMT network surrounding the k-fiber. In control, k-fibers exhibited both relaxation and residual displacement as observed at shorter timescales (**Figure 5F,G**). However, unfocused k-fibers that were manipulated and held strikingly exhibited permanent displacement compared to control (**Figure 5H,I**). Note that the shown unfocused k-fiber seems to break, which we occasionally observed in response to long pulls (Long et al. 2020). While k-fiber organization is known to be more variable and difficult to track in spindles lacking poles (Richter et al. 2023), we consistently saw permanent displacement and no relaxation of spindle fibers in long-held unfocused k-fibers, which was never observed in any other condition. This is consistent with pole-focusing forces being essential for structural recovery over a timescale of minutes.

Kinetochores-fiber relaxation can be quantified temporally and spatially

To measure dynamics of k-fiber relaxation after needle release, we analyzed the displacement curves following two minutes after release, a time at which we observed the manipulated regions of most k-fibers rejoin the displacement of their respective plus- and minus-ends (**Figure 5J**). Exponential decay curves were fit using SciPy to determine the dynamics of decay (**Figure 5K**). To test how well exponential decays fit k-fiber relaxation curves, we performed linear regression on the log-transformed y-coordinates from **Figure 5J** (**Figure supplement 9**). For all instances where k-fiber relaxation was observed, r-squared values were high (**Figure 5L**). Unfocused k-fibers held for long times exhibited poor exponential decay fits, consistent with no observed relaxation or elasticity (**Figure 5J,L**). Interestingly, the average half-life of decay was around 30 seconds for all conditions where k-fibers relaxed, similar to the half-life of non-kMTs in the spindle (**Figure 5M**, Saxton et al. 1984, Zhai et al. 1995). Additionally, the half-life is proportional to the ratio of a material's viscosity to elasticity. Force-calibrated needles are required for exact measures of viscosity and elasticity; however, it is intriguing that the ratio of viscosity to elasticity seems similar across k-fibers released after short holds regardless of poles and pole-focusing forces. Unfocused k-fibers exhibiting permanent displacement after long holds yielded low half-lives close to zero, as expected (**Figure 5M**). Thus, fitting exponential decays is a useful tool for quantifying k-fiber relaxation, supporting our observations that k-fibers relax at similar rates at short timescales regardless of pole-focusing forces and lose relaxation dynamics at longer timescales without pole-focusing forces.

Finally, to test spatial dynamics of k-fiber relaxation, we compared the magnitudes of displacement after needle release. Following 8 μm needle pulls, relaxing k-fibers recovered approximately 3-6 μm of this distance (**Figure 5N**). Normalizing recovered displacement to initial displacement confirmed that relaxing k-fibers only typically recovered 40-70% of their initial displacement (**Figure 5O**). The remaining distance was likely lost to spindle translation, global spindle remodeling or rotation, local remodeling of the k-fiber and its immediate environment, or a combination of these. Of these factors, spindle and k-fiber remodeling would indicate some plasticity inside the spindle in response to force, in addition to the likely viscoelastic response observed on this timescale. Control k-fibers showed hints of greater k-fiber displacements and distance recovered after long holds compared to short holds, though these results would need more repetitions (**Figure 5N,O**). Additionally, unfocused k-fibers may exhibit greater displacement and distance recovered after needle release (**Figure 5O,P**). One notable unfocused outlier k-fiber that was only initially pulled 4 μm and released instead of 8 μm (see † in J) exhibited the greatest displacement recovery to the point of overshooting its original position (**Figure 5O**). However, unfocused k-fibers did not recover any displacement after long holds, consistent with being stabilized at their new location (**Figure 5N,O**) and with pole-focusing forces being essential for long-term structural maintenance of the spindle.

In summary, control k-fibers exhibited partial relaxation after needle pulling and release on short and long timescales, consistent with exhibiting both plastic and viscoelastic responses at the tested forces. Unfocused k-fibers also exhibited partial relaxation at short timescales, but showed no displacement compared to control after

being held for a long time in a new location. These data are consistent with the timescale of the non-kMT spindle network remodeling over minutes to permanently stabilize the position of k-fibers in the absence of pole-focusing forces, though further experiments are needed to validate this model.

Figures

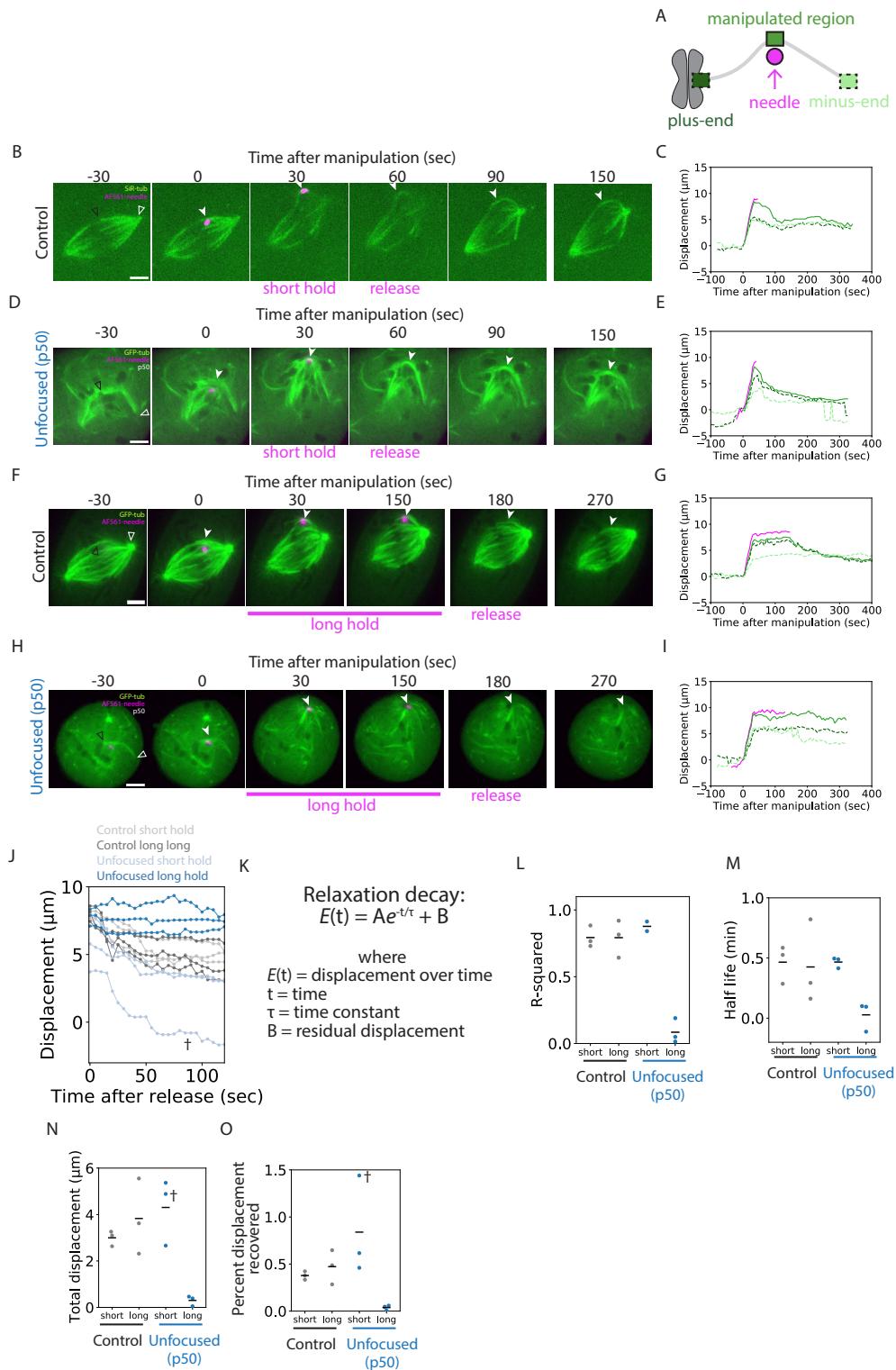


Figure 5. Kinetochore-fibers recover displacement from forces applied at short timescales, but permanently displace at longer timescales in the absence of poles and pole-focusing forces.

(Figure caption continued on the next page.)

(Figure caption continued from the previous page.)

(A) Schematic of a manipulated k-fiber. The plus-end is marked by the dark green dashed box, the minus-end by the light green dashed box, and the manipulated region by a green box. The needle is shown in pink. Movies are oriented and rotated to match, showing chromosomes and plus-ends to the left of the manipulated k-fiber, minus-ends to the right, with needle movement up along the y-axis. **(B)** Single z-plane images from a representative control k-fiber undergoing a 30-second needle manipulation across 8 μm followed by a quick needle release (short hold). For this and similar figures, white arrowheads follow the manipulated region along the k-fiber. Black-outlined arrowheads in the first time point mark the plus-end, white-outlined arrowheads the minus-end. Spindles were visualized using SiR-tubulin or GFP-tub and shown in green. Needles were dyed with AF-561 and shown in magenta. **(C)** Displacement of the k-fiber over time as measured from B with $t=0$ at the start of microneedle manipulation. Displacement was calculated based on the XY coordinates of the region at $t=0$, the XY coordinates at the region at every time, and the axis of needle displacement (see Methods). Needle displacement is plotted in magenta, the manipulated region in solid green, the plus-end in dashed dark green, and the minus-end in dashed light green. **(D)** Single z-plane images from a representative k-fiber in an unfocused (p50) spindle undergoing a 30-second needle manipulation across 8 μm followed by a quick needle release (short hold). **(E)** Displacement versus time calculated from D, plotted as described in C. **(F)** Single z-plane images from a representative control k-fiber undergoing a 30-second needle manipulation across 8 μm followed by a 2 minute hold and release (long hold). **(G)** Displacement versus time calculated from F, plotted as described in C. **(H)** Single z-plane images from a k-fiber in an unfocused (p50) spindle undergoing a 30-second needle manipulation across 8 μm followed by a 2 minute hold and release (long hold). Note that this k-fiber may have undergone breakage. **(I)** Displacement versus time calculated from H, plotted as described in C. **(J)** Displacement curves for all needle pulls performed, with $t=0$ at the time of needle release, ending at $t=120$, the subset of time used for subsequent calculations. Light gray traces represent control k-fibers with short holds, dark gray represent control k-fibers with long holds, light blue represent unfocused (p50) k-fibers with short holds, dark blue represent unfocused (p50) k-fibers with long holds. $n=3$ for all conditions. † denotes one outlier light blue trace that did not complete the full 8 μm pull in J,N, and O. Traces from J were plotted on a log scale and used to calculate linear regression (**Figure supplement 9**). **(K)** Relaxation function used to calculate exponential decay fits to data in J, where displacement is a function of time, the time constant τ , and constants A and B. Initial values for A, τ , and B were manually estimated and optimized using SciPy curve fitting (see Methods). **(L)** R-squared values from linear regression performed on log-transformed axes of J. (Control, short hold = 0.79 ± 0.08 , long hold = 0.79 ± 0.14 ; Unfocused, short hold = 0.88 ± 0.05 , long hold = 0.08 ± 0.09) (see Methods, **Figure supplement 9**)

(Figure caption continued on the next page.)

(Figure caption continued from the previous page.)

(M) Half-life of k-fiber relaxation from exponential decays fitted to curves from J. Half-life is the time constant τ calculated as in K multiplied by $\ln(2)$ (see Methods, **Figure supplement 9**). (Control, short hold = 0.47 ± 0.16 min, long hold = 0.43 ± 0.35 min; Unfocused, short hold = 0.47 ± 0.05 min, long hold = 0.28 ± 0.12 min) **(N)** Total displacement of manipulated region after needle release for control and unfocused k-fibers after short and long holds at $t=120$ s. (Control, short hold = 3.00 ± 0.33 μm , long hold = 3.83 ± 1.63 μm ; Unfocused, short hold = 4.31 ± 1.44 μm , long hold = 0.30 ± 0.22 μm) **(O)** Percent of displacement recovered after needle release, comparing displacement at $t=120$ s to displacement at $t=0$. (Control, short hold = 0.39 ± 0.04 , long hold = 0.47 ± 0.18 ; Unfocused, short hold = 0.84 ± 0.53 , long hold = 0.04 ± 0.03)

Supplemental Figures

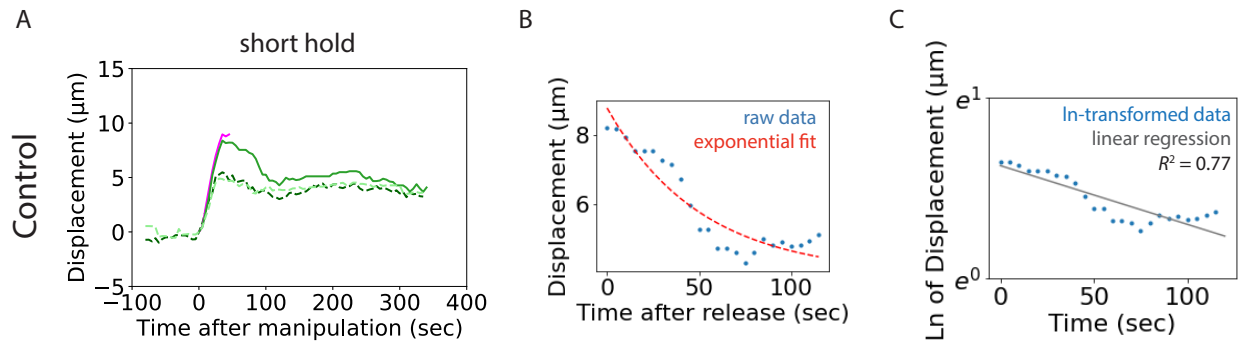


Figure supplement 9. Log transformation of axes and linear regression describes k-fiber relaxation curves.

Exponential fits and linear regression analysis are shown for one example trace from Figure 5. **(A)** Representative displacement of a manipulated control k-fiber after a short hold from Figure 5C. **(B)** Exponential decay fits to k-fiber displacement curves for the 2 minutes following needle release. Blue dots represent the raw data from A normalized to $t=0$ needle release plotted through $t=120$ sec. Red dashed line represents the exponential decay curve fit using SciPy (see Methods). **(C)** Axes from B were log-transformed for linear regression analysis (see Methods). Blue dots represent raw data from B transformed by natural log. Gray line represents linear regression analysis performed using SciPy with the resulting r-squared value shown.

Discussion and Outlook

These results, although preliminary, provide an exciting method for probing the local and global forces that anchor and organize k-fibers in the spindle to ensure proper architecture for chromosome segregation. Future work necessitates replication, but these experiments already provide key insights into k-fiber organization.

The response of k-fibers to prolonged forces in the absence of pole-focusing supports the model of poles as global organizers of k-fibers. Given that dynein is known to pull shortened k-fibers back into focused poles (Elting et al., 2014; Sikirzhytski et al., 2014) and that control but not unfocused k-fibers displace as spindles remodel after long needle holds (**Figure 5F,G**), it suggests that pole-focusing forces are responsible for actively organizing k-fibers on longer timescales. This model is consistent with the increased length and width observed in unfocused spindles (**Figure 1D**), the tendency for p50-overexpressing spindles to become more unfocused and spread out over time (**Figure 1A**), and the increased amount of misaligned k-fibers in unfocused spindles compared to control (**Figure supplement 6**). We speculate that k-fibers are roughly anchored in place on shorter timescales based on the viscoelasticity of the underlying spindle network, but active forces from motor proteins are required to properly position them on longer timescales. We further speculate that the spindle spreading observed in unfocused spindles may be due to stochastic movements that cause unfocused k-fibers to drift over long times, unable to be corrected by pole-focusing forces, but still become locally anchored in their new locations by the underlying spindle network. This is also consistent with the role of dynein and poles in providing spindle elasticity as well as coupling spindle length and width (Shimamoto et al., 2011). Thus, spindle pole-focusing

and local anchorage may work together to ensure robust k-fiber positioning across space and time.

Varying timescales and magnitudes of force applied can reveal different aspects of spindle material properties. We probed k-fibers on a timescale of force that has been shown to yield viscous responses in *Xenopus* (Itabashi et al. 2009). Consistent with this, we observed k-fiber relaxation in the two minutes following a 30 second needle pull and release, interestingly with similar half-lives of relaxation decay in the presence or absence of pole-focusing forces. We thus speculate that pole-focusing forces are negligible on shorter timescales of force applied to k-fibers whereby the surrounding spindle network can still provide a similar viscoelastic environment for the k-fiber to anchor it in place. With longer holds post-manipulation, however, we observed a striking difference between control and unfocused k-fibers, where control k-fibers exhibited some relaxation but unfocused k-fibers exhibited permanent displacement, or complete plasticity. At which time threshold does this transition from seemingly viscoelastic to fully plastic occur in unfocused spindles? Probing unfocused k-fiber relaxation with various needle hold times could reveal the timescale of when non-pole-focusing forces act on k-fibers, uncovering underlying mechanisms of k-fiber anchorage in the spindle independent of poles.

Directly measuring material properties in these experiments is challenging due to lacking absolute force measurements, as well as the observation that manipulated k-fiber regions did not fully recover displacement after needle release (**Figure 5O**). Furthermore, plus- and minus-ends also did not fully recover to their starting positions after needle releases (**Figure 5C,E,G,I**). This residual displacement is likely explained

by a combination of cell translation, spindle translation, spindle rotation, global spindle plasticity, or local k-fiber plasticity. Careful image registration that can accurately control for cell or spindle translations and rotations without introducing artifacts from global remodeling in control or unfocused spindles would allow evaluation of the alleged plasticity of k-fibers in response to force. However, the displacement of the manipulated region generally relaxed and reached a steady-state position close to the residual displacement of the plus- and minus-ends. This is consistent with a model whereby the applied force moved the k-fiber to a new steady-state location resulting from translation and remodeling, but where the k-fiber was still embedded in a viscoelastic network allowing for a smaller elastic contribution that led to relaxation of the manipulated region to rejoin the rest of the k-fiber in its new location. In fact, we may speculate that the total force applied was sufficient to enter the spindle's plastic regime based on hints from one outlier trace that only completed a 4 μm pull instead of the full 8 μm (see † in **Figure 5J,O**). This k-fiber may have experienced less overall force, causing less overall deformation that never reached a plastic regime. Thus, this k-fiber may have been manipulated just in the viscoelastic regime, allowing it to recover more of its initial displacement compared to k-fibers manipulated by greater forces. A compelling future direction would be to perform experiments at lower forces, that is, at shorter pull distances, to potentially reduce plasticity observed. Ultimately however, to directly calculate viscoelastic and elastic properties of k-fibers and spindles and disentangle them from plastic responses, needles would need to be force-calibrated to generate absolute force measurements - a technically challenging but powerful tool (Nicklas, 1983).

This work raises questions about the molecular mechanisms of k-fiber anchorage and spindle viscoelasticity. What is the source of k-fiber relaxation seen in control spindles and spindles lacking pole-focusing forces? We speculate on several non-mutually exclusive models that may contribute to a viscoelastic response of k-fibers to force: underlying non-kMT networks, spindle crosslinkers, motor proteins, contractile actin networks, internal k-fiber viscoelasticity, and cytoplasmic flows.

It is known that microtubules *in vitro* can generate elastic networks, likely explained by weak interactions between filaments (Lin et al. 2007), and non-kMT density has been shown to directly contribute to spindle viscosity and elasticity (Shimamoto et al., 2011). K-fibers are embedded in a meshwork of non-kMTs that turn over on the ~30 second timescale (McDonald et al., 1992, Saxton et al. 1984, Zhai et al. 1995), likely connected mechanically by crosslinkers (Elting et al., 2017; Steblyanko et al., 2020), though it is not known what this network looks like in unfocused spindles. Electron tomography would be a powerful tool to characterize the location and potential connections between MTs in unfocused spindles. However, this underlying network of non-kMTs is an enticing model to describe our results, since we observed no relaxation of unfocused k-fibers at times that would allow this network to fully remodel and potentially anchor the k-fiber at a new site (**Figure 5H,I,J**). To directly probe the effect of the non-kMT network on k-fiber anchorage, we propose to treat spindles with low doses of nocodazole to selectively depolymerize non-kMTs but not k-fibers (Cassimeris and Salmon, 1991). Pulling and releasing k-fibers in these spindles will probe the contribution of non-kMTs to anchorage and viscoelastic responses of k-fibers.

Spindle crosslinkers and motor proteins have been shown to likely play a major role in contributing to spindle viscosity and elasticity (Shimamoto et al., 2011), as well as providing local load-bearing and weak mechanical coupling laterally along k-fibers (Elting et al., 2017, Suresh et al., 2020). We propose performing needle release experiments in spindles with either increased crosslinking, such as by treating with FCPT to rigor bind crosslinker Eg5 (Groen et al., 2008), or decreasing crosslinking, such as by performing NuMA RNAi (Elting et al., 2017), to probe the contribution of crosslinkers on k-fiber relaxation dynamics. We can also perform needle release experiments in doubly-inhibited spindles, where dynein and Eg5 are simultaneously inhibited to yield a bipolar but mechanically defective spindle (Shimamoto et al., 2011; Neahring et al., 2021) to disentangle the role of pole structures from forces produced by motor proteins Eg5 and dynein on k-fiber anchorage.

Intrinsically, polymers can exhibit elasticity at lower forces, that is, reversible deformations after forces applied, and plasticity at higher forces, that is, irreversible deformations due to molecular rearrangements. Thus, it is possible that the material properties of k-fibers themselves result in their observed responses to force. This is challenging to assay directly, since k-fibers are not able to be reconstituted *in vitro*. Instead, we could treat spindles with low-dose nocodazole and p50 overexpression to reduce k-fiber connections to poles and non-kMT networks, isolating the k-fiber as much as possible, then probe their response to force to get closer to characterizing intrinsic k-fiber material properties. Additionally, we can examine curvature profiles of k-fibers over time during needle manipulation and release, assaying whether k-fibers recover their shape after deformations from force. This can provide hints of elastic and plastic

deformations of k-fibers with or without pole-focusing forces. K-fiber dynamics may also play a role in responses to force and recovering from displacements or deformations, which can be probed by manipulating taxol-treated k-fibers whose dynamics have stopped. Manipulating k-fibers in kinetochore mutants that change the average number of kMTs in a k-fiber can also probe the effects of intrinsic k-fiber material properties and composition on responses to force (Kuhn et al., 2019). Actin has been found to play a role in spindle assembly and positioning (Kunda and Baum, 2009). In theory, contractile actin networks outside the spindle can provide elastic force to hold the spindle in place and could also be remodeling during long holds. Depolymerizing actin with Latrunculin B and probing the spindle's response to force from microneedle manipulation can test what actin contributes elastically.

Finally, cytoplasmic flows are known to provide forces that can position spindles and provide viscous drag on spindle elements (Nicklas 1982, Xie et al. 2022). Thus, it is possible that cytoplasmic viscosity contributes to k-fiber relaxation after needle pulls, though it is difficult to assay directly. Cytoplasmic flows can be mapped using cytoplasmic fiducial markers such as QDOTs (Barroso 2011) to correlate with k-fiber movement.

While these experiments can elucidate individual k-fiber anchorage mechanisms in the spindle, they can also provide a method that measures global, not just local, anchorage in the spindle - how are different k-fibers connected across the spindle independently of poles, and how does this network dissipate force? We can compare the movement of neighbor k-fibers near and far from the manipulated k-fiber to ask whether force is dissipated locally or globally in the absence of pole-focusing forces

compared to control, testing what lateral or end anchorage exists independent of poles. Examining curvature profiles of manipulated unfocused k-fibers may also provide information about where the k-fiber is experiencing force during pulls, if there is any localized anchorage along k-fibers independent of pole-focusing, and even estimating the force that manipulated k-fibers are under using modeling.

Anchorage of k-fibers ends in the absence of pole-focusing is also intriguing, especially whether unfocused k-fiber minus-ends are able to exhibit local anchorage when not connected to a pole. However, it is difficult to decouple the effects of viscosity and anchorage on holding k-fiber ends in place - imagine pulling on the central part of a piece of string in a pot of honey; its ends may look like they are anchored in place, but that may merely be a result of viscous drag. Curvature profile analysis of manipulated k-fiber may provide hints of end anchorage. Testing response to needle manipulation while varying needle position along an unfocused k-fiber may reveal local differences in anchorage or material properties along the k-fiber. For example, pulling near the plus-end may probe viscous forces felt by chromosomes. Pulling near minus-ends may more directly test minus-end anchorage in the absence of poles. This can be especially powerful if using force-calibrated needles to test whether different positions along a k-fiber are anchored by different magnitudes of force. Finally, we can measure the length of unfocused k-fibers over time during needle manipulation. Control k-fibers are known to elongate in response to long needle pulls (Long et al. 2020), which can lead to force dissipation and may explain the difference in displacements of the k-fiber's manipulated region compared to its plus- and minus-ends.

Though our preliminary experiments are able to address intriguing questions of spindle organization, they are challenging experiments that require additional controls. p50-overexpressing spindles exhibit variability in k-fiber length, position, dynamics, and coordination (Richter et al., 2023). It is unknown whether k-fiber composition is similar between unfocused and control spindles, and it can be difficult to determine where unfocused k-fibers start and end, especially in a single z-plane as imaged during needle pulls. Performing z-stacks of spindles before and after needle manipulation can help ensure we capture the entirety of the k-fiber and confirm that it is connected to chromosomes. Furthermore, the example unfocused k-fiber in the long hold (**Figure 5H**) seems to undergo breakage, which can affect its material properties, even though no displacement was observed after needle release, similar to other replicates in this condition. Additional repetitions are needed to confirm that k-fiber breakage does not affect the lack of relaxation observed. To additionally verify our results, we can pull on the same k-fiber multiple times under different conditions to control for cell-to-cell or k-fiber-to-k-fiber variability.

Overall, our results are consistent with a speculative model whereby spindles use different strategies to respond to shorter and longer forces in order to robustly maintain their shape and organize k-fibers. On the seconds timescale of force applied, the underlying non-kMT network and its crosslinkers provide local anchorage, enabling a viscoelastic response of k-fibers to force, keeping them roughly anchored in place. On the minutes timescale of force applied, this non-kMT network may remodel around a displaced k-fiber to stabilize it in a new location when pole-focusing forces are absent. Thus, k-fiber anchorage could locally self-organize to provide viscoelastic reinforcement

against short-term disruptive forces, but global organization forces are still required on longer timescales to spatially coordinate spindle components in their viscoelastic environment.

Chapter 4. Functional coordination of kinetochore-fibers in the mammalian spindle

Introduction

So far, we have shown that while a focused pole is not required for setting or maintaining k-fiber lengths (**Figure 1, Figure 2**), it is required for global spindle coordination (**Figure 1, Figure 5**) and robust k-fiber dynamics (**Figure 3, Figure 4**). So what do spindle poles contribute to mitotic spindles? Proper regulation of the mitotic spindle ensures equal division of chromosomes into two daughter cells, so we assayed the functional requirement of spindle poles on chromosome segregation and cell division.

Results

Spindle poles coordinate chromosome segregation and cytokinesis

To test the functional output of focused spindle poles in mammalian cells, we treated control and unfocused spindles with reversine, an MPS1 inhibitor that forces mitotic cells to enter anaphase, even in the absence of dynein activity required for spindle assembly checkpoint satisfaction (Santaguida et al., 2010). Control and unfocused spindles were imaged through anaphase after reversine addition using a

single z-plane (**Figure 6A, Video 9**) and also imaged with z-stacks encompassing the whole spindle once before adding reversine, and 20 min after anaphase onset (**Figure 6B**). In spindles without focused poles, chromatids separated—albeit at twofold reduced velocities compared to control—in the separating chromatid pairs that could be identified (**Figure 6C**). In the absence of poles or dynein activity, such chromatid separation likely comes from pushing from the spindle center rather than from pulling from the cell cortex (Vukušić et al., 2017; Yu et al., 2019).

However, major segregation and cytokinetic defects were observed in these cells compared to control, consistent with segregation defects observed in k-fibers disconnected from poles (Toorn et al., 2022; Sivaram et al., 2009). Cytokinetic defects and the presence of multiple cytokinetic furrows frequently resulted in the formation of more than two daughter cells in unfocused spindles (**Figure 6D**). Furthermore, chromosome masses were scattered and unequally distributed in these cells, whereby control daughter cells inherited approximately half of the chromosome mass as measured by DNA intensity, but not daughter cells of unfocused spindles (**Figure 6E**). Given that focused mammalian spindles lacking dynein pole-focusing forces and lacking Eg5 proceed through anaphase with much milder defects than we observe here (Neahring et al., 2021), we conclude that poles, rather than dynein-based pole-focusing forces, are primarily responsible for these defects. Thus, while many species lack spindle poles, and while unfocused mammalian spindles can still maintain k-fiber length and separate chromatids, spindle poles are essential to coordinate chromosome segregation and cytokinesis in mammalian cells.

Figures

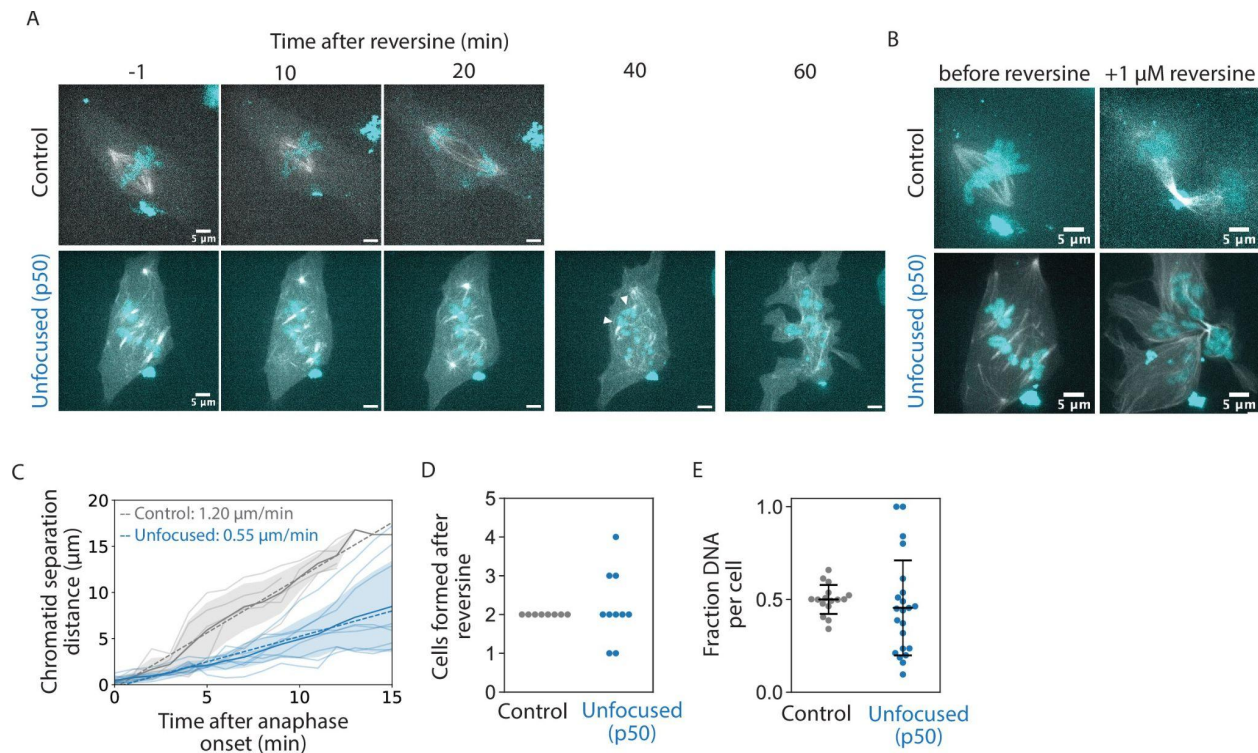


Figure 6. Spindle poles coordinate chromosome segregation and cytokinesis.

See also **Video 9**. **(A)** Representative confocal timelapse images of Ptk2 spindles with GFP- α -tubulin (in control and unfocused) and mCherry-p50 (in unfocused only) treated with 0.1 or 0.5 μ M SiR-DNA with 1 μ M reversine added at $t = 0$. Arrowheads depict an example of sister chromatids separating, later measured in C. **(B)** Max-intensity z-projections before adding reversine and 20 min after anaphase onset for the control and unfocused spindle in A. C-E are from the same dataset. (Control: $N = 8$ dividing cells; Unfocused: $N = 10$ dividing cells). **(C)** Sister chromatid separation velocity. For the chromatid pairs that were observed to separate, sister chromatid distance over time was measured for focused and unfocused spindles starting at anaphase onset. Control is plotted in gray, unfocused in blue. Light-colored traces represent one separating chromatid pair, with their average plotted as a dark line with shading representing ± 1 standard deviation. The line of best fit for each condition averaged is shown as a dotted line, with their slopes shown. (Control: $N = 4$ dividing cells, $n = 5$ chromosome pairs, separation velocity = 1.20 μ m/min; Unfocused: $N = 3$ dividing cells, $n = 9$ chromatid pairs, separation velocity = 0.55 μ m/min). **(D)** Number of “cells” formed after cytokinesis in reversine-treated control and unfocused spindles. (Control: 2 ± 0 cells; Unfocused: 2.20 ± 0.87 “cells”). **(E)** Fraction of chromosome mass per “cell” after reversine treatment. Summed z-projections of chromosome masses were used to calculate the fraction of chromosome mass per cell. (Control: 0.50 ± 0.08 a.u.; Unfocused: 0.45 ± 0.26 a.u.). Numbers are mean \pm standard deviation.

Supplemental Figures

Video 9. A reversine-treated control spindle undergoing anaphase: control vs unfocused spindle.

Control (left) and unfocused (right) spindles treated with a cell cycle checkpoint inhibitor enter anaphase and segregate chromosomes. See also **Figure 6A**. Live confocal imaging of a PtK2 cell labeled with SiR-DNA (cyan) and expressing GFP- α -tubulin and mCherry-p50 (unfocused only) with 1 μ M reversine added. Time is in min:sec, with reversine added at t = 0. Scale bar, 5 μ m.

Discussion

Here, we show that in the mammalian spindle, individual k-fibers set and maintain their lengths locally but require the global cue of a focused pole to coordinate their lengths across space and time (**Figure 7**). Our work reveals that pole-less spindles can set and maintain k-fibers at the same mean length as in control, recovering their steady-state lengths if acutely shortened, but they have impaired dynamics and coordination and are unable to properly segregate chromosomes. We propose a model whereby length is an emergent property of individual k-fibers in the spindle, and where spindle poles ensure that this network of k-fibers is highly dynamic and coordinated across space and time to ultimately cluster chromatids into two future daughter cells. While this work provides insight into k-fiber length establishment and maintenance, what local mechanisms set the k-fiber's length scale remains an open question. We discuss three models. First, concentration gradients centered on chromosomes (Kalab and Heald, 2008; Wang et al., 2011) could in principle set a distance-dependent activity threshold for spindle proteins that regulate k-fiber dynamics and length. However, it is unclear whether such a gradient with correct length scale and function exists in mammalian spindles. Also, while the globally disorganized structure of unfocused spindles (**Figure 1B,D**) could lead to modified gradients, the mean length of k-fibers is unchanged and length does not correlate with spatial position along both spindle axes (**Figure 1E, Figure supplement 6**). Second, a lifetime model (Burbank et al., 2007; Conway et al., 2022) stipulates that length is proportional to microtubule lifetime and the velocity of poleward transport, and is sufficient to predict spindle length in spindles with a tiled array of short microtubules. While the length distribution of individual

microtubules in unfocused k-fibers is unknown, this model would predict an exponential distribution of microtubule lengths within a k-fiber (Brugués et al., 2012), inconsistent with electron microscopy in control PtK cells (McDonald et al., 1992). Moreover, we observed a more than 4-fold reduced (and near zero) flux velocity in unfocused spindles (**Figure 3D**), which only a dramatic increase in lifetime could compensate for in this lifetime model. Finally, an “antenna” model (Varga et al., 2006) stipulates that longer k-fibers recruit more microtubule dynamics regulators since they have a longer microtubule antenna to land on. For example, in mammalian spindles, the microtubule depolymerase Kif18A binds k-fibers in a length-dependent way and exhibits length-dependent depolymerase activity, being more active on long k-fibers and thereby shortening them (Mayr et al., 2007; Stumpff et al., 2008). Given that this local antenna model is consistent with our current observations, testing in unfocused spindles whether k-fiber growth rate indeed changes with k-fiber length and testing the role of dynamics regulators in length establishment and maintenance represent important future directions.

Our findings suggest that in response to length changes, k-fibers regulate their plus-end dynamics in an analog manner and their minus-end dynamics in a digital manner. In unfocused spindles, we have shown that the regrowth of shortened k-fibers is driven by an increase in plus-end polymerization, and that this occurs in response to length changes, not simply dynein-based force changes (**Figure 4**). Consistently, longer k-fibers grow more slowly than shorter ones in a titratable manner in human spindles (Conway et al., 2022). The regulation mechanisms above are all analog in nature. In turn, after ablation, we always observed a near-absence of minus-end dynamics. This

reduction in flux was only large enough in control k-fibers to observe statistical significance, though unfocused k-fibers appeared to follow the same trend (**Figure 4C, D**). This is consistent with a switchlike mechanism turning depolymerization on or off, proposed on the basis that tension on k-fibers turns off apparent minus-end depolymerization (Dumont and Mitchison, 2009a; Long et al., 2020). The mechanism behind such digital regulation is not known. One possibility is that a proximal pole structure is required to recruit active microtubule depolymerases, such as Kif2a (Gaetz and Kapoor, 2004; Ganem et al., 2005), to k-fiber minus-ends. In unfocused spindles without a pole, k-fibers would be less dynamic (**Figure 3D**) based on having fewer depolymerases at their minus-ends. In physical perturbation experiments where k-fibers are separated from the pole center, their apparent minus-end depolymerization would stop (Dumont and Mitchison, 2009a; Long et al., 2020) based on a too-distant depolymerase pool and thus fewer depolymerases at minus-ends. Interestingly, Kif2a can drive spindle scaling in *Xenopus* meiotic spindles (Wilbur and Heald, 2013).

In principle, the concomitant loss of dynein-mediated pole-focusing forces and spindle poles makes it difficult to disentangle the role of each in regulating spindle coordination, maintenance, and function in our findings. However, recent work has revealed that mammalian spindles can achieve similar architecture whether or not dynein (or its recruiter NuMA) is knocked out (Neahring et al., 2021). This suggests that the severe defects in spindle coordination (**Figure 1, Figure 5, Figure 6**) and maintenance (**Figure 2**) observed in p50-unfocused spindles are more likely due to the loss of spindle poles than due to the loss of dynein activity per se. Though we cannot exclude it, this also suggests that the findings we make in unfocused spindles are not

due changes in activity of the dynein population at kinetochores. Additionally, centrosomes are disconnected from the spindle (**Videos 2,3**), ruling out contributions from centrosomes (Khodjakov et al., 2000) or astral microtubules on k-fiber length regulation at metaphase. Mammalian spindle poles are also required for spindle positioning (Kiyomitsu and Cheeseman, 2012) and have been proposed to help segregate centrosomes (Friedländer and Wahrman, 1970). More work is needed to understand the evolution and function of spindle poles across species and, more broadly, the diversity of spindle architectures across evolution.

Lastly, our work provides compelling preliminary evidence for probing the role of poles and pole-focusing forces on k-fiber organization and anchorage. We observe hints that k-fibers can form local anchorages that confer elasticity on short timescales independently of poles, but pole-focusing forces are necessary to reorganize k-fibers on longer timescales. Overall, we show that microneedle manipulation of focused and unfocused k-fibers is a powerful tool to probe spindle material properties, connectivity, and anchorage, that can be combined with different molecular contexts, timescales, and magnitudes of force to elucidate the underlying mechanisms of how spindles are built to dynamically yet robustly organize k-fibers.

We propose that this biological blueprint, where k-fibers locally set and maintain their individual length and poles coordinate them globally, robustly builds a complex yet dynamic spindle. For example, we've shown that while k-fibers establish their mean lengths locally, global cues homogenize them (**Figure 1E, 1G**). We put forward the idea that the structural integrity and flexible remodeling of other higher-order structures may also rely on individual parts having all the necessary intrinsic information and self-

organization to get the correct linear architecture, with global cues organizing these parts in space and time. More broadly, our work highlights how self-organization at local scales and coordination at global scales can work together to build emergent complex biological structures.

Figures

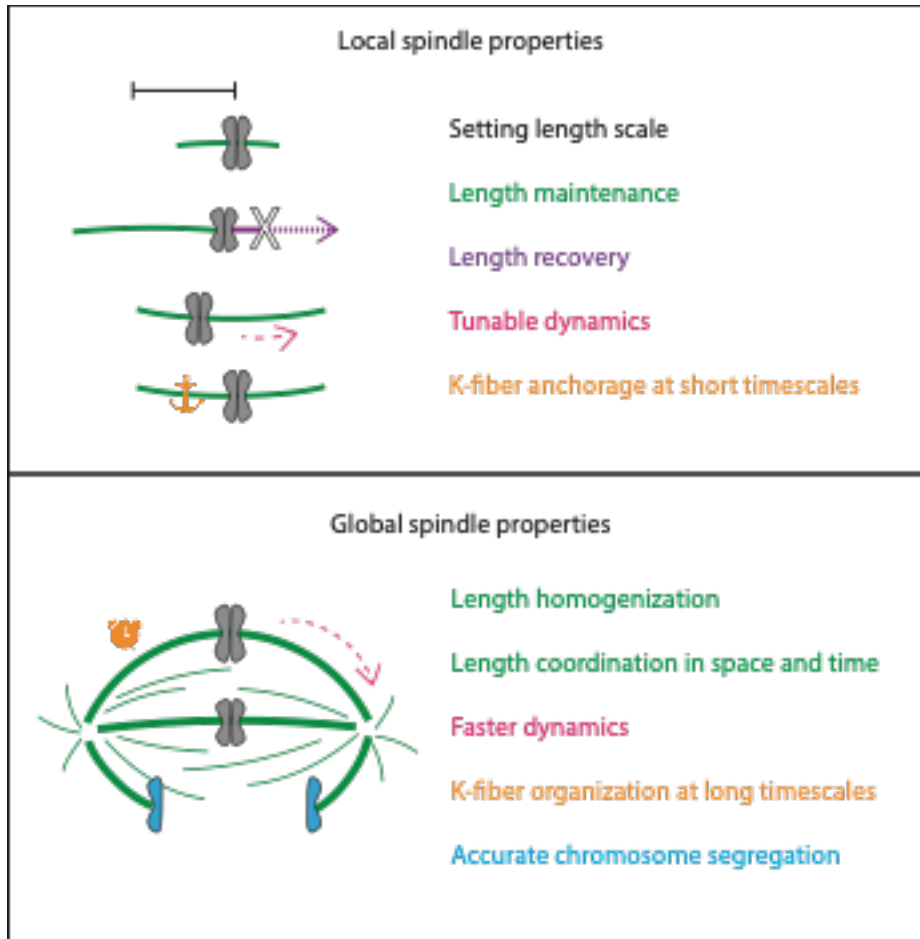


Figure 7. Spindle length is a local spindle property and length coordination is a global spindle property.

Cartoon summary of spindle properties set locally versus globally. Setting, maintaining, and recovering length is regulated by individual k-fibers locally, independently of poles and pole-focusing forces. In turn, coordinating lengths across space and longer timescales requires global cues from focused poles. In sum, spindle length emerges locally, but spindle coordination emerges globally.

Materials and Methods

Table 1. Key resources used in this work.

Reagent type (species) or resource	Designation	Source or reference	Identifiers	Additional information
Cell line (P. tridactylus, male)	PtK2	gift from T. Mitchison, Harvard University	PMID: 1633624	Kidney epithelial
Cell line (P. tridactylus, male)	HaloTag-tubulin PtK2	This paper		Kidney epithelial
Cell line (H. sapiens, female)	RPE1	ATCC	ATCC Cat#CRL-4000; RRID: CVCL_4388	Retina, epithelial
Chemical compound, drug	Nocodazole	Sigma	M1404	Final concentration 2 μ M
Chemical compound, drug	Reversine	Sigma	R3904	Final concentration 1 μ M
Chemical compound, drug	Viafect	ProMega	E4981	1:6 ratio of Viafect:DNA used
Chemical compound, drug	Janelia Fluor 646	Janelia	6148	Final concentration 100 nM
Chemical compound, drug	SiR-DNA	Spirochrome	SC007	Final concentration 0.1-0.5 μ M with 1 μ M verapamil
Chemical compound, drug	SiR-tubulin	Spirochrome	SC002	Final concentration 0.1 μ M with 1 μ M verapamil

Reagent type (species) or resource	Designation	Source or reference	Identifiers	Additional information
Recombinant DNA reagent	pLV- β -tubulin-HaloTag (plasmid)	This paper		Lentiviral plasmid. Progenitors: Addgene #114021 (Geert Kops) and Addgene #64691 (Yasushi Okada)
Recombinant DNA reagent	pLV-mCherry-p50 (plasmid)	This paper		Lentiviral plasmid. Progenitors: Addgene #114021 (Geert Kops) and mCherry-p50 (PMID: 19196984)
Recombinant DNA reagent	eGFP- α -tubulin (plasmid)	Michael Davidson collection given to UCSF	Addgene Plasmid #56450	(Rizzo et al., 2009)
Recombinant DNA reagent	mCherry-p50 (plasmid)	Gift from M. Meffert, Johns Hopkins University	PMID: 19196984	(Shrum et al., 2009)
Recombinant DNA reagent	β -tubulin HaloTag (plasmid)	Addgene	Addgene Plasmid #64691	(Uno et al., 2014)
Software, algorithm	FIJI	FIJI	ImageJ version 2.1.0	(Schindelin et al., 2012)
Software, algorithm	Wolfram Mathematica	Wolfram Mathematica	Version 13.0	
Software, algorithm	MetaMorph	MDS Analytical Technologies	Version 7.8	
Software, algorithm	Micro-Manager	Micro-Manager	Version 2.0.0	(Edelstein et al., 2010)
Software, algorithm	Python	Python	Version 3.8.1	Spyder IDE version 4.1.5

Cell biology and microscopy

Cell culture

All work herein was performed using wild-type PtK2 cells (*P. tridactylus*, male, PMID: 1633624, kidney epithelial, gift from Tim Mitchison, Harvard University) unless otherwise stated. PtK2 cells were cultured in MEM (11095; Thermo Fisher, Waltham, MA) supplemented with sodium pyruvate (11360; Thermo Fisher), non-essential amino acids (11140; Thermo Fisher), penicillin/streptomycin, and 10% heat-inactivated fetal bovine serum (10438; Thermo Fisher). The cell line tested negative for mycoplasma, and while we did not authenticate it, its cell behavior and growth characteristics were similar to those reported for the parental PtK2 cell line, whose transcriptome we sequenced (Udy et al., 2015). Cells were maintained at 37 °C and 5% CO₂. hTERT-RPE1 cells (*H. sapiens*, female, ATCC Cat#CRL-4000, RRID: CVCL_4388, retinal epithelial) were cultured in DMEM/F12 with GlutaMAX (11320; Thermo Fisher) supplemented with penicillin/streptomycin and 10% FBS. This cell line was not authenticated by STR profiling but tested negative for mycoplasma.

To visualize microtubules, PtK2 cells were transfected with eGFP- α -tubulin (Clontech) using Viafect (Promega) unless otherwise noted. To inhibit dynein, PtK2 or RPE1 cells were additionally transfected or lentivirally infected with mCherry-p50 (a gift from Mollie Meffert, Johns Hopkins University; Shrum et al., 2009). Transient transfections were prepared in a 100 μ l reaction mix per 35 mm dish, including a 1:6 ratio of DNA to Viafect, OptiMEM media up to 100 μ l, and eGFP- α -tubulin (0.7 μ g) or both eGFP- α -tubulin (0.4 μ g) and mCherry-p50 (0.5 μ g), and added 3-4 days prior to imaging.

Lentiviral plasmids and cell line construction

The coding sequences of β -tubulin-HaloTag (Addgene #64691) and mCherry-p50 were cloned into a puromycin-resistant lentiviral vector (Addgene #114021) using Gibson assembly. Lentivirus for each construct was produced in HEK293T cells. To generate the stable polyclonal β -tubulin-HaloTag PtK2 cell line (**Figure 1A**), wild-type PtK2 cells were infected with β -tubulin-HaloTag virus and selected using 5 μ g/ml puromycin. Because p50 overexpression disrupts cell division, mCherry-p50 lentivirus was used to transiently infect each 35mm dish 3-4 days prior to imaging (**Figure 1A**).

Imaging

PtK2 or RPE1 cells were plated on 35 mm #1.5 coverslip glass-bottom dishes coated with poly-D-lysine (MatTek, Ashland, MA) and imaged. The cells were maintained at 30-37 °C in a stage top incubator (Tokai Hit, Fujinomiya-shi, Japan). Two similar inverted spinning-disk confocal (CSU-X1; Yokogawa Electric Corporation) microscopes (Eclipse TI-E; Nikon) with the following components were used for live-cell imaging: head dichroic Semrock Di01-T405/488/561/647, head dichroic Semrock Di01-T405/488/561, 100x 1.45 Ph3 oil objective, a 60X 1.4 Ph3 oil objective, 488 nm (100, 120, or 150 mW), 561 nm (100 or 150 mW) and 642 (100mW) nm diode lasers, emission filters ET525/36M (Chroma Technology) for GFP, ET630/75M for mCherry, and ET690/50M for JF 646 (Chroma Technology), a perfect focus system (Nikon, Tokyo, Japan), an iXon3 camera (Andor Technology, 105 nm/pixel using 100X objective at bin = 1), and a Zyla 4.2 sCMOS camera (Andor Technology, 65.7 nm/pixel using 100X objective at bin = 1). For imaging, 400 ms exposures were used for phase contrast and 50–100 ms exposures were used for fluorescence. Cells were imaged at

30°C (by default) or 37°C to speed up slower processes (**Figure 1A, Figure 2G,H and Figure 6**), 5% CO₂ in a closed, humidity-controlled Tokai Hit PLAM chamber. Cells were imaged via MetaMorph (7.8, MDS Analytical Technologies) or Micro-Manager (2.0.0).

Spindle assembly videos (**Figure 1A, Videos 1,2**) were captured using a 60x objective for a wider field of view, selecting approximately 20 stage positions and imaging overnight at 37°C for 8-10 hours. To capture unfocused spindle assembly, positions containing cells expressing moderate-to-high levels of mCherry-p50 relative to other cells on the dish were selected. Spindles over time were imaged with 1 µm z-slices every minute to avoid photodamage (**Figure 1A, Figure 1H**). Volumetric spindle images were taken using a 100X objective, with z-slices 0.3 µm apart encompassing the whole spindle (**Figure 1B, Figure 6B, Figure supplement 7**). To visualize DNA, 0.1-0.5 µM SiR-DNA (Spirochrome) with 1 µM verapamil were added at least 30 min prior to imaging (**Figure 6**). To visualize microtubules, 100 nM JF 646 was added to HaloTag-tub PtK2 cells at least 30 min prior to imaging (**Figure 1A**). Videos are displayed with optima brightness and contrast for viewing.

Photobleaching and laser ablation (Figure 2,3,4)

Photobleaching and laser ablations were performed using 514 or 551 nm ns-pulsed laser light and a galvo-controlled MicroPoint Laser System (Andor, Oxford Instruments) operated through MetaMorph or Micro-Manager. Single z-planes were chosen to pick the clearest k-fiber visible from plus- to minus-end, parallel to the coverslip, that was long enough to ablate. Non-ablated unfocused k-fibers in the same imaging plane were not necessarily parallel to the coverslip, so their full length was not always captured in the single z-plane due to tilt. Photobleaching was performed by firing

the laser at the lowest possible power to make a visible bleach mark (~20% of total power), whereas ablations were performed at the lowest possible power to fully cut a k-fiber (~60% of total power). K-fiber ablations were verified by observing complete depolymerization of newly created plus-ends, relaxation of interkinetochore distance, or poleward transport of k-fiber stubs (control only). When firing the laser, 1-3 areas around the region of interest were targeted and hit with 5-20 pulses each. Ablations were imaged using one z-plane every 12 s to assay short-term dynamics, then switching to every 1 min after approximately 10 min following ablation to avoid phototoxicity.

Nocodazole washout (Figure 2)

Z-planes containing the highest number of clearly distinguishable k-fibers, that were parallel to the coverslip, were chosen for imaging. 2 μ M nocodazole was swapped into dishes using a transfer pipet while imaging. After 10 min to depolymerize microtubules, dishes were washed 10X in prewarmed media to remove nocodazole and allow spindle reassembly. Spindles were imaged at one z-plane every min to avoid phototoxicity during spindle recovery. To measure k-fiber lengths before nocodazole addition, individual k-fiber traces were averaged over time before drug addition (\leq 10 min). K-fiber lengths after drug washout were averaged over time after spindles reached a steady-state length (\geq 10 min), subtracting centrosome radius for control k-fibers during these times.

Reversine treatment (Figure 6)

Metaphase spindles were volumetrically imaged with a z-step of 0.3 μm across whole live spindles before reversine addition. The media was then swapped to similar media containing 1 μM reversine and imaged at a single z-plane. 20 min after anaphase onset, cells were again imaged volumetrically as previously described.

Microneedle manipulation (Figure 5)

Microneedles were made, bent, and coated as described in Suresh et al. 2020. Microneedles were mounted and positioned as described in Suresh et al. 2020, but were positioned along a k-fiber and moved approximately perpendicularly to the k-fiber for 30 seconds for a total needle displacement of 8 μm in most cases (see outlier marked by † in **Figure 5**). The needle was then raised out of the cell either immediately or after two minutes.

Image analysis and statistics

Image analysis

Feature tracking, spindle architecture measurements, and statistical analyses were done in FIJI and Python unless otherwise stated. Videos and images are displayed with optimal brightness and contrast for viewing.

Spindle major and minor axes length (Figure 1D, Figure supplement 4)

Spindle minor and major axes lengths were determined by cropping, rotating, then thresholding spindle images with the Otsu filter using SciKit. Ellipses were fitted to

thresholded spindles to approximate the length of their major and minor axes using SciKit's region properties measurement (**Figure supplement 4A**). In control spindles, the major axis corresponded to spindle length along the pole-to-pole axis, and the minor axis corresponded to spindle width along the metaphase plate axis. However, unfocused spindles were disorganized along both axes to the extent where the minor axis did not always correspond to the metaphase plate axis. Thus, **Figure 1D** reports "spindle minor axis length" and "spindle major axis length" rather than "spindle width" and "spindle length". Furthermore, it is worth noting that in unfocused spindles, spindle length is decoupled from k-fiber length because of k-fiber disorganization along both axes. Thus, spindle length was not measured in unfocused spindles, but individual k-fiber length was measured as described below.

K-fiber length (Figure 1,2, Figure supplement 4B,C)

For k-fiber length measurements at a single time point, z-stacks of live spindles were taken with a step size of 0.3 μm across the entire spindle (Figure 1B). Individual k-fibers were measured using a maximum intensity z-projection of only the slices where that k-fiber was in focus (**Figure supplement 4B**). Line profiles were then measured by drawing ROIs in FIJI with a spline fit line of width 15 pixels, spanning from plus-ends at the start of tubulin intensity next to the chromosome towards minus-ends, using the minimum number of points to recapitulate the curve of the k-fiber (**Figure supplement 4B**). The 3D length was then estimated with the Pythagorean theorem, using the length of the k-fiber's ROI and the z-height of the slices it spanned (**Figure 1E-G, Figure supplement 4C**). For control k-fibers, the end of the ROI spanning the k-fiber was defined as the center of the pole, and centrosome radius was subtracted to estimate

true k-fiber length (**Figure 1E-G, I-N, Figure 2C-F, H, I**). Since minus-ends of focused k-fibers are not distinguishable in a pole and typically terminate within 2 μm of centrosomes (McDonald et al., 1992), centrosome radius was approximated by drawing line scans through focused poles and measuring the half width at half max intensity (**Figure supplement 5**). This approximation was used for all subsequent length measurements. For unfocused and ablated k-fibers, minus-ends were defined as the farthest point of visible tubulin intensity corresponding to that k-fiber. Lengths of ROIs were calculated and plotted in Python. K-fiber lengths over time were measured as described above, but from videos with single imaging planes or from max intensity projections based on a step size of 1 μm across the volume of the spindle. K-fiber lengths were then measured using ROIs of width 5 pixels for k-fibers whose plus- and minus-ends were visible across at least 5 frames (k-fiber lengths over time, **Figure 1H-N** and ablated k-fibers, **Figure 2C-F**). K-fiber lengths were binned by minute for aggregate analyses.

In k-fibers following ablation, centrosome size was subtracted only when control k-fibers were reincorporated into the pole and the ablated minus-end was no longer visible. To calculate growth rates for k-fiber lengths over time, linear regression was performed using SciPy on binned k-fiber lengths for those with data at time points 0-6 minutes. One control k-fiber was excluded from growth rate analysis based on these criteria.

Spatial correlation analysis (Figure supplement 6)

K-fiber positions in spindles were quantified latitudinally and longitudinally, then correlated to length. To approximate the metaphase plate axis, a line of best fit was

drawn through kinetochore positions in a cell as approximated by the positions of k-fiber plus-ends. Only the positions of k-fiber plus-ends whose sister k-fibers were also measured were used to calculate spindle axes. In control spindles, the metaphase plate axis corresponded to the spindle width axis. The long spindle axis was determined by drawing a line perpendicular to the metaphase plate axis through the average kinetochore position. In control spindles, this long spindle axis corresponded to the pole-to-pole axis. Distance from each k-fiber's plus-end to the long axis was measured, and then binned into "inner" k-fibers if $\leq 2 \mu\text{m}$ and "outer" if $\geq 3 \mu\text{m}$.

Alignment scores were calculated based on the distance from each k-fiber's plus end to the metaphase plate axis, and then given either a negative or positive sign depending on whether the k-fiber was "over-aligned" (see yellow control example in **Figure supplement 6B**) with longer expected lengths or "under-aligned" (see blue control example in **Figure supplement 6B**). K-fibers were categorized as either over- or under-aligned based on the relative positions of their plus- and minus-ends. If both ends were on the same side of the metaphase plate, i.e. the k-fiber was under-aligned and fully on one side of the metaphase plate, the distance from the plus-end to the metaphase plate was recorded as positive. If the plus- and minus-ends were on opposite sides of the metaphase plate axis, i.e. the k-fiber was over-aligned and crossing the metaphase plate axis, the distance from the plus-end to the metaphase plate was recorded as negative. A perfectly aligned pair of kinetochores would each have an alignment score of approximately +1. This method of assigning alignment scores was sufficient to accurately categorize all control k-fibers as over- or under-aligned. However, there were rare extreme cases of disorganization in unfocused

spindles that miscategorized them 3.77% of the time, e.g. where a k-fiber was “over-aligned” but both of its ends were on the far side of the metaphase plate. Manually correcting these rare cases yielded correlation coefficients -0.33 for control (unchanged) and -0.17 for unfocused (compared to -0.18 reported in the figure).

Tracking photobleach marks along k-fibers (Figure 3, 4)

Spindles of k-fibers with photobleach marks were registered by the tub-GFP channel to account for global spindle translations and rotations. Videos of ablated k-fibers were not registered due to expected translocation of k-fibers stubs after ablation. All videos were trimmed to be isochronous, then flipped, rotated, and cropped so that individual k-fibers with photomarks were latitudinal, with chromosomes on the left and minus-ends on the right. A line with width 5 pixels was drawn along individual k-fibers, and the max intensity projection along the height at each time point was plotted to generate kymographs. Segmented lines were drawn along the kymographs corresponding to the positions of the kinetochore, photomark, and minus-end or pole over time. The distance between the mark and the minus-end over time was calculated and plotted in Python.

Displacement calculations (Figure 5)

Total k-fiber displacement was calculated by tracking movies from **Figure 5B,D,F,H**. Manipulated regions (white arrowhead), needle position (magenta), plus-ends (black empty arrowhead), and minus-ends (white empty arrowhead) were tracked using mTrackJ in FIJI. The distance between the XY coordinates at the start of needle manipulation and the XY coordinates of the tracked region at every time point were

calculated in Python and plotted in **Figure 5C,E,G,I**. To roughly assign a sign to displacement, positive displacement was defined as y movement up along the y-axis as defined by the trajectory of the needle, where negative displacement represents the tracked region going below the y coordinate at the start of manipulation, that is, if the region were to “overshoot” its original position. Movies were rotated so that the needle movement was always straight up vertically. Note that this rough displacement calculation occasionally yields artifacts in the plus- and minus-end displacement tracks as observed in **Figure 5E**. Just before 300 seconds, the minus-end trace appears to jump long distances between positive and negative displacement. A future displacement measurement could rely on vectorial analysis to rigorously calculate positive and negative displacement, yielding fewer artifacts. However, none of the manipulated region traces exhibited these artifacts (**Figure 5J**), allowing for valid calculations in **Figure 5L-O**. Displacement curves were then translated in **Figure 5J**, normalized so that $t=0$ corresponded to the time of needle release.

Exponential curve fitting (Figure 5)

Displacement curves from **Figure 5J** were fitted with exponential decays in Python. The exponential decay function shown in Figure 5K was fed manually-determined initial parameters A , τ , and B and optimized using the SciPy function `scipy.optimize.curve_fit` to yield the curves as represented in **Figure supplement 9B**. Half-life was calculated based on the optimized τ values $\times \ln(2)$ (**Figure 5M**).

Log axis transformation and linear regression (Figure 5, Figure supplement 9)

To evaluate and compare exponential fits, data from **Figure 5J** were plotted on log-transformed axes to perform linear regression. The y-axis (Displacement) from **Figure 5J** was transformed by natural log and plotted in **Figure supplement 9C** (blue points), then linear regression was performed in Python using `linregress` from SciPy (gray line) to yield R-squared values plotted in **Figure 5L**. Note that log transforms cannot be used for negative data, and one outlier trace (marked by † in **Figure 5J**) exhibited negative displacement. This outlier is thus excluded from **Figure 5L**. However, an exponential decay could still be fit to this curve.

Cell division analysis (Figure 6)

Quantifications of cell division were performed in FIJI. Chromatid separation was quantified by tracking distance between sister chromatids, specifically between the plus-ends of their attached k-fibers, starting the frame before chromatid separation was first observed and ending at the onset of cytokinesis marked by the appearance of a cleavage furrow. To quantify the fraction of chromosome mass per daughter “cell”, “cell” outlines were drawn based on phase contrast images, and the overlap of each cell outline with the summed intensity z-projection of chromosome masses was measured.

Statistical analysis

Statistical analyses were performed in Python using NumPy and SciPy unless otherwise stated. Linear regression and Pearson’s correlation coefficient calculations were performed using SciPy. In the text, whenever we state a significant change or

difference, the p-value for those comparisons was less than 0.05. In figures, * indicates $p < 0.05$, ** $p < 0.005$, and *** $p < 0.0005$. In the figure legends, we display the exact p-value from every statistical test made. We used a two-tailed Welch's t-test everywhere unless otherwise stated, since this compares two independent datasets with different standard deviations. Legends include n , the number of individual measurements made, and N , the number of unique cells assayed for each condition.

Autocorrelation (Figure 3A)

Autocorrelation analysis was performed using Wolfram Mathematica 13.0. The autocorrelation is calculated by the built-in function "CorrelationFunction". By this definition, the autocorrelation of a k-fiber at lag h is $\frac{\sum_{i=1}^{n-h} (x_i - \bar{x})(x_{i+h} - \bar{x})}{\sum_{i=1}^n (x_i - \bar{x})^2}$ where x_i is k-fiber length at time i and \bar{x} is the mean of x_i . The standard deviation is calculated by the built-in function "StandardDeviation". Statistical significance was performed using the built-in function "LocationTest" at each h .

Script packages

All scripts were written in Python using Spyder through Anaconda unless otherwise stated. Pandas was used for data organization, SciPy for statistical analyses, Matplotlib and seaborn for plotting and data visualization, SciKit for image analysis, and NumPy for general use. FIJI was used for video formatting, intensity quantification, kymograph generation, and tracking k-fibers.

Video preparation

Videos show a single spinning disk confocal z-slice imaged over time (**Video 4, Video 5, Video 6, Video 7, Video 8, Video 9**) or a maximum intensity projection (**Video 1, Video 2, Video 3**) and were formatted for publication using FIJI and set to play at 10 fps.

References

- Akiyoshi B, Sarangapani KK, Powers AF, Nelson CR, Reichow SL, Arellano-Santoyo H, Gonen T, Ranish JA, Asbury CL, Biggins S. 2010. Tension directly stabilizes reconstituted kinetochore-microtubule attachments. *Nature* 468:576–579. DOI: <https://doi.org/10.1038/nature09594>, PMID: 21107429
- Barroso, M. M. Quantum Dots in Cell Biology. *J Histochem Cytochem* **59**, 237–251 (2011).
- Blangy, A. *et al.* Phosphorylation by p34cdc2 regulates spindle association of human Eg5, a kinesin-related motor essential for bipolar spindle formation in vivo. *Cell* **83**, 1159–1169 (1995).
- Brugués J, Nuzzo V, Mazur E, Needleman DJ. 2012. Nucleation and transport organize microtubules in metaphase spindles. *Cell* 149:554–564. DOI: <https://doi.org/10.1016/j.cell.2012.03.027>, PMID: 22541427
- Burbank KS, Mitchison TJ, Fisher DS. 2007. Slide-and-cluster models for spindle assembly. *Current Biology* 17:1373–1383. DOI: <https://doi.org/10.1016/j.cub.2007.07.058>, PMID: 17702580
- Cameron LA, Yang G, Cimini D, Canman JC, Kisurina-Evgenieva O, Khodjakov A, Danuser G, Salmon ED. 2006. Kinesin 5-independent poleward flux of kinetochore microtubules in PtK1 cells. *The Journal of Cell Biology* 173:173–179. DOI: <https://doi.org/10.1083/jcb.200601075>, PMID: 16636143
- Cassimeris, L. & Salmon, E. D. Kinetochore microtubules shorten by loss of subunits at the kinetochores of prometaphase chromosomes. *Journal of Cell Science* **98**, 151–158 (1991).

- Compton DA. 1998. Focusing on spindle poles. *Journal of Cell Science* 111 (Pt 11):1477–1481. DOI: <https://doi.org/10.1242/jcs.111.11.1477>, PMID: 9580556
- Conway W, Kiewisz R, Fabig G, Kelleher CP, Wu HY, Anjur-Dietrich M, Müller-Reichert T, Needleman DJ. 2022. Self-organization of kinetochore-fibers in human mitotic spindles. *eLife* 11:e75458. DOI: <https://doi.org/10.7554/eLife.75458>, PMID: 35876665
- Dechant R, Glotzer M. 2003. Centrosome separation and central spindle assembly act in redundant pathways that regulate microtubule density and trigger cleavage furrow formation. *Developmental Cell* 4:333–344. DOI:[https://doi.org/10.1016/s1534-5807\(03\)00057-1](https://doi.org/10.1016/s1534-5807(03)00057-1), PMID: 12636915
- DeLuca JG, Gall WE, Ciferri C, Cimini D, Musacchio A, Salmon ED. 2006. Kinetochore microtubule dynamics and attachment stability are regulated by Hec1. *Cell* 127:969–982. DOI: <https://doi.org/10.1016/j.cell.2006.09.047>, PMID: 17129782
- Dudka D, Castrogiovanni C, Liaudet N, Vassal H, Meraldi P. 2019. Spindle-length-dependent HURP localization allows Centrosomes to control kinetochore-fiber plus-end dynamics. *Current Biology* 29:3563–3578. DOI: <https://doi.org/10.1016/j.cub.2019.08.061>, PMID: 31668617
- Dumont J, Petri S, Pellegrin F, Terret ME, Bohnsack MT, Rassinier P, Georget V, Kalab P, Gruss OJ, Verlhac MH. 2007. A centriole- and RanGTP-independent spindle assembly pathway in meiosis I of vertebrate oocytes. *The Journal of Cell Biology* 176:295–305. DOI: <https://doi.org/10.1083/jcb.200605199>, PMID: 17261848

- Dumont S, Mitchison TJ. 2009a. Compression regulates mitotic spindle length by a mechanochemical switch at the poles. *Current Biology* 19:1086–1095. DOI: <https://doi.org/10.1016/j.cub.2009.05.056>, PMID: 19540117
- Dumont S, Mitchison TJ. 2009b. Force and length in the mitotic spindle. *Current Biology* 19:R749–R761. DOI: <https://doi.org/10.1016/j.cub.2009.07.028>, PMID: 19906577
- Echeverri CJ, Paschal BM, Vaughan KT, Vallee RB. 1996. Molecular characterization of the 50-kD subunit of dynactin reveals function for the complex in chromosome alignment and spindle organization during mitosis. *The Journal of Cell Biology* 132:617–633. DOI: <https://doi.org/10.1083/jcb.132.4.617>, PMID: 8647893
- Edelstein A, Amodaj N, Hoover K, Vale R, Stuurman N. 2010. Computer control of microscopes using μ Manager. *Current Protocols in Molecular Biology* Chapter 14:Unit14. DOI: <https://doi.org/10.1002/0471142727.mb1420s92>, PMID: 20890901
- Elting MW, Hueschen CL, Udy DB, Dumont S. 2014. Force on spindle microtubule minus ends moves chromosomes. *The Journal of Cell Biology* 206:245–256. DOI: <https://doi.org/10.1083/jcb.201401091>, PMID:25023517
- Elting MW, Prakash M, Udy DB, Dumont S. 2017. Mapping load-bearing in the mammalian spindle reveals local kinetochore fiber anchorage that provides mechanical isolation and redundancy. *Current Biology* 27:2112– 2122.. DOI: <https://doi.org/10.1016/j.cub.2017.06.018>, PMID: 28690110
- Foster, P. J., Fürthauer, S., Shelley, M. J. & Needleman, D. J. Active contraction of microtubule networks. *eLife* 4, e10837 (2015).

- Friedländer M, Wahrman J. 1970. The spindle as a basal body distributor. A study in the meiosis of the male silkworm moth, *Bombyx mori*. *Journal of Cell Science* 7:65–89. DOI: <https://doi.org/10.1242/jcs.7.1.65>, PMID: 5529252
- Gaetz J, Kapoor TM. 2004. Dynein/dynactin regulate metaphase spindle length by targeting depolymerizing activities to spindle poles. *The Journal of Cell Biology* 166:465–471. DOI: <https://doi.org/10.1083/jcb.200404015>, PMID: 15314063
- Gaglio T, Dionne MA, Compton DA. 1997. Mitotic spindle poles are organized by structural and motor proteins in addition to centrosomes. *The Journal of Cell Biology* 138:1055–1066. DOI: <https://doi.org/10.1083/jcb.138.5.1055>, PMID: 9281583
- Ganem NJ, Compton DA. 2004. The KinI kinesin Kif2a is required for bipolar spindle assembly through a functional relationship with MCAK. *The Journal of Cell Biology* 166:473–478. DOI: <https://doi.org/10.1083/jcb.200404012>, PMID: 15302853
- Ganem NJ, Upton K, Compton DA. 2005. Efficient mitosis in human cells lacking poleward microtubule flux. *Current Biology* 15:1827–1832. DOI: <https://doi.org/10.1016/j.cub.2005.08.065>, PMID: 16243029
- Good MC, Vahey MD, Skandarajah A, Fletcher DA, Heald R. 2013. Cytoplasmic volume modulates spindle size during embryogenesis. *Science* 342:856–860. DOI: <https://doi.org/10.1126/science.1243147>, PMID: 24233724
- Gorbsky GJ, Borisy GG. 1989. Microtubules of the kinetochore fiber turn over in metaphase but not in anaphase. *The Journal of Cell Biology* 109:653–662. DOI: <https://doi.org/10.1083/jcb.109.2.653>, PMID: 2668301

- Goshima G, Saitoh S, Yanagida M. 1999. Proper metaphase spindle length is determined by centromere proteins Mis12 and Mis6 required for faithful chromosome segregation. *Genes & Development* 13:1664–1677. DOI: <https://doi.org/10.1101/gad.13.13.1664>, PMID: 10398680
- Goshima G, Nédélec F, Vale RD. 2005a. Mechanisms for focusing mitotic spindle poles by minus end–directed motor proteins. *The Journal of Cell Biology* 171:229–240. DOI: <https://doi.org/10.1083/jcb.200505107>, PMID: 16247025
- Goshima G, Wollman R, Stuurman N, Scholey JM, Vale RD. 2005b. Length control of the metaphase spindle. *Current Biology* 15:1979–1988. DOI: <https://doi.org/10.1016/j.cub.2005.09.054>, PMID: 16303556
- Goshima G, Scholey JM. 2010. Control of mitotic spindle length. *Annual Review of Cell and Developmental Biology* 26:21–57. DOI: <https://doi.org/10.1146/annurev-cellbio-100109-104006>, PMID: 20604709
- Grill, S. W. & Hyman, A. A. Spindle positioning by cortical pulling forces. *Dev Cell* **8**, 461–465 (2005).
- Grishchuk, E. L. & McIntosh, J. R. Microtubule depolymerization can drive poleward chromosome motion in fission yeast. *EMBO J* **25**, 4888–4896 (2006).
- Groen, A. C. *et al.* A novel small-molecule inhibitor reveals a possible role of kinesin-5 in anastral spindle-pole assembly. *J Cell Sci* **121**, 2293–2300 (2008).
- Guild J, Ginzberg MB, Hueschen CL, Mitchison TJ, Dumont S. 2017. Increased lateral microtubule contact at the cell cortex is sufficient to drive mammalian spindle elongation. *Molecular Biology of the Cell* 28:1975–1983. DOI: <https://doi.org/10.1091/mbc.E17-03-0171>, PMID: 28468979

- Hazel J, Krutkramelis K, Mooney P, Tomschik M, Gerow K, Oakey J, Gatlin JC. 2013. Changes in cytoplasmic volume are sufficient to drive spindle scaling. *Science* 342:853–856. DOI: <https://doi.org/10.1126/science.1243110>, PMID: 24233723
- Heald R, Tournebise R, Blank T, Sandaltzopoulos R, Becker P, Hyman A, Karsenti E. 1996. Self-organization of microtubules into bipolar spindles around artificial chromosomes in *Xenopus* egg extracts. *Nature* 382:420–425. DOI: <https://doi.org/10.1038/382420a0>, PMID: 8684481
- Howell BJ, McEwen BF, Canman JC, Hoffman DB, Farrar EM, Rieder CL, Salmon ED. 2001. Cytoplasmic dynein/ dynactin drives kinetochore protein transport to the spindle poles and has a role in mitotic spindle checkpoint inactivation. *The Journal of Cell Biology* 155:1159–1172. DOI: <https://doi.org/10.1083/jcb.200105093>, PMID: 11756470
- Hueschen CL, Kenny SJ, Xu K, Dumont S. 2017. NuMA recruits dynein activity to microtubule minus-ends at mitosis. *eLife* 6:e29328. DOI: <https://doi.org/10.7554/eLife.29328>, PMID: 29185983
- Hueschen CL, Galstyan V, Amouzgar M, Phillips R, Dumont S. 2019. Microtubule end-clustering maintains a steady-state spindle shape. *Current Biology* 29:700–708. DOI: <https://doi.org/10.1016/j.cub.2019.01.016>, PMID: 30744975
- Itabashi, T. *et al.* Probing the mechanical architecture of the vertebrate meiotic spindle. *Nat Methods* 6, 167–172 (2009).
- Kajtez J, Solomatina A, Novak M, Polak B, Vukušić K, Rüdiger J, Cojoc G, Milas A, Šumanovac Šestak I, Risteski P, Tavano F, Klemm AH, Roscioli E, Welburn J, Cimini D, Glunčić M, Pavin N, Tolić IM. 2016. Overlap microtubules link sister K-

- fibres and balance the forces on bi-oriented kinetochores. *Nature Communications* 7:10298. DOI: <https://doi.org/10.1038/ncomms10298>, PMID: 26728792
- Kajtez, J. *et al.* Overlap microtubules link sister k-fibres and balance the forces on bi-oriented kinetochores. *Nat Commun* 7, 10298 (2016).
- Kalab P, Heald R. 2008. The RanGTP gradient - a GPS for the mitotic spindle. *Journal of Cell Science* 121:1577– 1586. DOI: <https://doi.org/10.1242/jcs.005959>, PMID: 18469014
- Kapitein, L. C. *et al.* The bipolar mitotic kinesin Eg5 moves on both microtubules that it crosslinks. *Nature* **435**, 114–118 (2005).
- Khodjakov A, Cole RW, Oakley BR, Rieder CL. 2000. Centrosome-independent mitotic spindle formation in vertebrates. *Current Biology* 10:59–67. DOI: [https://doi.org/10.1016/s0960-9822\(99\)00276-6](https://doi.org/10.1016/s0960-9822(99)00276-6), PMID: 10662665
- Kiewisz R, Fabig G, Conway W, Baum D, Needleman D, Müller-Reichert T. 2022. Three-dimensional structure of kinetochore-fibers in human mitotic spindles. *eLife* 11:e75459. DOI: <https://doi.org/10.7554/eLife.75459>, PMID: 35894209
- Kiyomitsu T, Cheeseman IM. 2012. Chromosome- and spindle-pole-derived signals generate an intrinsic code for spindle position and orientation. *Nature Cell Biology* 14:311–317. DOI: <https://doi.org/10.1038/ncb2440>, PMID: 22327364
- Koshland, D. E., Mitchison, T. J. & Kirschner, M. W. Polewards chromosome movement driven by microtubule depolymerization in vitro. *Nature* **331**, 499–504 (1988).
- Kuhn, J. & Dumont, S. Mammalian kinetochores count attached microtubules in a sensitive and switch-like manner. *J Cell Biol* **218**, 3583–3596 (2019).

Kunda, P. & Baum, B. The actin cytoskeleton in spindle assembly and positioning.

Trends in Cell Biology **19**, 174–179 (2009).

Lacroix B, Letort G, Pitayu L, Sallé J, Stefanutti M, Maton G, Ladouceur AM, Canman

JC, Maddox PS, Maddox AS, Minc N, Nédélec F, Dumont J. 2018. Microtubule dynamics scale with cell size to set spindle length and assembly timing.

Developmental Cell 45:496–511.. DOI: [https://doi.org/10.1016/j.devcel.2018.04.](https://doi.org/10.1016/j.devcel.2018.04.022)

022, PMID: 29787710

Lecland N, Lüders J. 2014. The dynamics of microtubule minus ends in the human

mitotic spindle. *Nature Cell Biology* 16:770–778. DOI:

<https://doi.org/10.1038/ncb2996>, PMID: 24976384

Lin, Y.-C., Koenderink, G. H., MacKintosh, F. C. & Weitz, D. A. Viscoelastic Properties

of Microtubule Networks. *Macromolecules* **40**, 7714–7720 (2007).

Long AF, Suresh P, Dumont S. 2020. Individual kinetochore-fibers locally dissipate

force to maintain robust mammalian spindle structure. *The Journal of Cell*

Biology 219:e201911090. DOI: <https://doi.org/10.1083/jcb.201911090>, PMID:

32435797

Maiato H, Rieder CL, Khodjakov A. 2004. Kinetochore-driven formation of kinetochore

fibers contributes to spindle assembly during animal mitosis. *The Journal of Cell*

Biology 167:831–840. DOI: <https://doi.org/10.1083/jcb.200407090>, PMID:

15569709

Mastrorarde, D. N., McDonald, K. L., Ding, R. & McIntosh, J. R. Interpolar spindle

microtubules in PTK cells. *Journal of Cell Biology* **123**, 1475–1489 (1993).

- Matos I, Pereira AJ, Lince-Faria M, Cameron LA, Salmon ED, Maiato H. 2009. Synchronizing chromosome segregation by flux-dependent force equalization at kinetochores. *The Journal of Cell Biology* 186:11–26. DOI: <https://doi.org/10.1083/jcb.200904153>, PMID: 19581410
- Mayr MI, Hümmer S, Bormann J, Grüner T, Adio S, Woehlke G, Mayer TU. 2007. The human kinesin Kif18A is a motile microtubule depolymerase essential for chromosome congression. *Current Biology* 17:488–498. DOI: <https://doi.org/10.1016/j.cub.2007.02.036>, PMID: 17346968
- McDonald KL, O'Toole ET, Mastronarde DN, McIntosh JR. 1992. Kinetochores microtubules in PTK cells. *The Journal of Cell Biology* 118:369–383. DOI: <https://doi.org/10.1083/jcb.118.2.369>, PMID: 1629239
- Merdes A, Ramyar K, Vechio JD, Cleveland DW. 1996. A complex of NuMA and cytoplasmic dynein is essential for mitotic spindle assembly. *Cell* 87:447–458. DOI: [https://doi.org/10.1016/s0092-8674\(00\)81365-3](https://doi.org/10.1016/s0092-8674(00)81365-3), PMID: 8898198
- Milas A, Tolić I. 2016. Relaxation of interkinetochore tension after severing of a K-fiber depends on the length of the K-fiber stub. *Matters Select* 2297–9239. DOI: <https://doi.org/10.19185/matters.201603000025>
- Mitchison TJ. 1989. Polewards microtubule flux in the mitotic spindle: evidence from photoactivation of fluorescence. *The Journal of Cell Biology* 109:637–652. DOI: <https://doi.org/10.1083/jcb.109.2.637>, PMID: 2760109
- Neahring L, Cho NH, Dumont S. 2021. Opposing motors provide mechanical and functional robustness in the human spindle. *Developmental Cell* 56:3006–3018. DOI: <https://doi.org/10.1016/j.devcel.2021.09.011>, PMID: 34614397

- Nicklas RB, Staehly CA. 1967. Chromosome micromanipulation. I. The mechanics of chromosome attachment to the spindle. *Chromosoma* 21:1–16. DOI: <https://doi.org/10.1007/BF00330544>, PMID: 5339860
- Nicklas, R. B., Kubai, D. F. & Hays, T. S. Spindle microtubules and their mechanical associations after micromanipulation in anaphase. *Journal of Cell Biology* **95**, 91–104 (1982).
- O’Toole E, Mophew M, McIntosh JR. 2020. Electron tomography reveals aspects of spindle structure important for mechanical stability at metaphase. *Molecular Biology of the Cell* 31:184–195. DOI: <https://doi.org/10.1091/mbc.E19-07-0405>, PMID: 31825721
- Quintyne NJ, Gill SR, Eckley DM, Crego CL, Compton DA, Schroer TA. 1999. Dynactin is required for microtubule anchoring at centrosomes. *The Journal of Cell Biology* 147:321–334. DOI: <https://doi.org/10.1083/jcb.147.2.321>, PMID: 10525538
- Rieckhoff EM, Berndt F, Elsner M, Golfier S, Decker F, Ishihara K, Brugués J. 2020. Spindle scaling is governed by cell boundary regulation of microtubule nucleation. *Current Biology* 30:4973–4983.. DOI: <https://doi.org/10.1016/j.cub.2020.10.093>, PMID: 33217321
- Richter, M. Probing cytoskeletal remodelling by cutting and marking filaments. *Nat Rev Mol Cell Biol* **25**, 83–83 (2024).
- Rizzo MA, Davidson MW, Piston DW. 2009. Fluorescent protein tracking and detection: fluorescent protein structure and color variants. *Cold Spring Harbor Protocols* 2009:pdb.top63. DOI: <https://doi.org/10.1101/pdb.top63>, PMID: 20150100

- Roostalu J, Rickman J, Thomas C, Nédélec F, Surrey T. 2018. Determinants of polar versus nematic organization in networks of dynamic microtubules and mitotic motors. *Cell* 175:796–808.. DOI: <https://doi.org/10.1016/j.cell.2018.09.029>, PMID: 30340043
- Santaguida S, Tighe A, D'Alise AM, Taylor SS, Musacchio A. 2010. Dissecting the role of MPS1 in chromosome biorientation and the spindle checkpoint through the small molecule inhibitor reversine. *The Journal of Cell Biology* 190:73–87. DOI: <https://doi.org/10.1083/jcb.201001036>, PMID: 20624901
- Saxton, W. M. *et al.* Tubulin dynamics in cultured mammalian cells. *The Journal of cell biology* **99**, 2175–2186 (1984).
- Schindelin J, Arganda-Carreras I, Frise E, Kaynig V, Longair M, Pietzsch T, Preibisch S, Rueden C, Saalfeld S, Schmid B, Tinevez JY, White DJ, Hartenstein V, Eliceiri K, Tomancak P, Cardona A. 2012. Fiji: an open-source platform for biological-image analysis. *Nature Methods* 9:676–682. DOI: <https://doi.org/10.1038/nmeth.2019>, PMID: 22743772
- Sharp DJ, Rogers GC, Scholey JM. 2000. Cytoplasmic dynein is required for poleward chromosome movement during mitosis in *Drosophila* embryos. *Nature Cell Biology* 2:922–930. DOI: <https://doi.org/10.1038/35046574>, PMID: 11146657
- Shimamoto, Y., Maeda, Y. T., Ishiwata, S., Libchaber, A. J. & Kapoor, T. M. Insights into the Micromechanical Properties of the Metaphase Spindle. *Cell* **145**, 1062–1074 (2011).
- Shrum CK, Defrancisco D, Meffert MK. 2009. Stimulated nuclear translocation of NF-kappaB and shuttling differentially depend on dynein and the dynactin complex.

PNAS 106:2647–2652. DOI: <https://doi.org/10.1073/pnas.0806677106>, PMID: 19196984

Sikirzhyski V, Magidson V, Steinman JB, He J, Le Berre M, Tikhonenko I, Ault JG, McEwen BF, Chen JK, Sui H, Piel M, Kapoor TM, Khodjakov A. 2014. Direct kinetochore-spindle pole connections are not required for chromosome segregation. *The Journal of Cell Biology* 206:231–243. DOI: <https://doi.org/10.1083/jcb.201401090>, PMID: 25023516

Silk AD, Holland AJ, Cleveland DW. 2009. Requirements for NuMA in maintenance and establishment of mammalian spindle poles. *The Journal of Cell Biology* 184:677–690. DOI: <https://doi.org/10.1083/jcb.200810091>, PMID: 19255246

Sivaram MVS, Wadzinski TL, Redick SD, Manna T, Doxsey SJ. 2009. Dynein light intermediate chain 1 is required for progress through the spindle assembly checkpoint. *The EMBO Journal* 28:902–914. DOI: <https://doi.org/10.1038/emboj.2009.38>, PMID: 19229290

So C, Menelaou K, Uraji J, Harasimov K, Steyer AM, Seres KB, Bucevičius J, Lukinavičius G, Möbius W, Sibold C, Tandler-Schneider A, Eckel H, Moltrecht R, Blayney M, Elder K, Schuh M. 2022. Mechanism of spindle pole organization and instability in human oocytes. *Science* 375:eabj3944. DOI: <https://doi.org/10.1126/science.abj3944>, PMID: 35143306

Steblyanko Y, Rajendraprasad G, Osswald M, Eibes S, Jacome A, Geley S, Pereira AJ, Maiato H, Barisic M. 2020. Microtubule poleward flux in human cells is driven by the coordinated action of four kinesins. *The EMBO Journal* 39:e105432. DOI: <https://doi.org/10.15252/emboj.2020105432>, PMID: 33073400

- Stumpff J, von Dassow G, Wagenbach M, Asbury C, Wordeman L. 2008. The kinesin-8 motor Kif18A suppresses kinetochore movements to control mitotic chromosome alignment. *Developmental Cell* 14:252–262. DOI: <https://doi.org/10.1016/j.devcel.2007.11.014>, PMID: 18267093
- Suresh, P., Long, A. F. & Dumont, S. Microneedle manipulation of the mammalian spindle reveals specialized, short-lived reinforcement near chromosomes. *eLife* **9**, e53807 (2020).
- Udy DB, Voorhies M, Chan PP, Lowe TM, Dumont S. 2015. Draft de novo transcriptome of the rat kangaroo *Potorous tridactylus* as a tool for cell biology. *PLOS ONE* 10:e0134738. DOI: <https://doi.org/10.1371/journal.pone.0134738>, PMID: 26252667
- Uno S-N, Kamiya M, Yoshihara T, Sugawara K, Okabe K, Tarhan MC, Fujita H, Funatsu T, Okada Y, Tobita S, Urano Y. 2014. A spontaneously blinking fluorophore based on intramolecular spirocyclization for live-cell super-resolution imaging. *Nature Chemistry* 6:681–689. DOI: <https://doi.org/10.1038/nchem.2002>, PMID: 25054937
- van Toorn M, Gooch A, Boerner S, Kiyomitsu T. 2022. NuMA deficiency causes micronuclei via checkpoint- insensitive k-fiber minus-end detachment from mitotic spindle poles. *bioRxiv*. DOI: <https://doi.org/10.1101/2022.10.04.510904>
- Varga V, Helenius J, Tanaka K, Hyman AA, Tanaka TU, Howard J. 2006. Yeast kinesin-8 depolymerizes microtubules in a length-dependent manner. *Nature Cell Biology* 8:957–962. DOI: <https://doi.org/10.1038/ncb1462>, PMID: 16906145

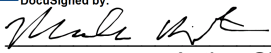
- Vladimirou, E. *et al.* Nonautonomous movement of chromosomes in mitosis. *Dev Cell* **27**, 60–71 (2013).
- Vukušić K, Buđa R, Bosilj A, Milas A, Pavin N, Tolić IM. 2017. Microtubule sliding within the bridging fiber pushes kinetochore fibers apart to segregate chromosomes. *Developmental Cell* 43:11–23.. DOI: <https://doi.org/10.1016/j.devcel.2017.09.010>, PMID: 29017027
- Wan X, Cimini D, Cameron LA, Salmon ED. 2012. The coupling between sister kinetochore directional instability and oscillations in centromere stretch in metaphase PtK1 cells. *Molecular Biology of the Cell* 23:1035–1046. DOI: <https://doi.org/10.1091/mbc.E11-09-0767>, PMID: 22298429
- Wang E, Ballister ER, Lampson MA. 2011. Aurora B dynamics at centromeres create a diffusion-based phosphorylation gradient. *The Journal of Cell Biology* 194:539–549. DOI: <https://doi.org/10.1083/jcb.201103044>, PMID: 21844210
- Waters JC, Mitchison TJ, Rieder CL, Salmon ED. 1996. The kinetochore microtubule minus-end disassembly associated with poleward flux produces a force that can do work. *Molecular Biology of the Cell* 7:1547–1558. DOI: <https://doi.org/10.1091/mbc.7.10.1547>, PMID: 8898361
- Wilbur JD, Heald R. 2013. Mitotic spindle scaling during *Xenopus* development by kif2a and importin α . *eLife* 2:e00290. DOI: <https://doi.org/10.7554/eLife.00290>, PMID: 23425906
- Wühr M, Chen Y, Dumont S, Groen AC, Needleman DJ, Salic A, Mitchison TJ. 2008. Evidence for an upper limit to mitotic spindle length. *Current Biology* 18:1256–1261. DOI: <https://doi.org/10.1016/j.cub.2008.07.092>, PMID: 18718761

- Yamada M, Goshima G. 2017. Mitotic spindle assembly in land plants: molecules and mechanisms. *Biology* 6:6. DOI: <https://doi.org/10.3390/biology6010006>, PMID: 28125061
- Yang G, Houghtaling BR, Gaetz J, Liu JZ, Danuser G, Kapoor TM. 2007. Architectural dynamics of the meiotic spindle revealed by single-fluorophore imaging. *Nature Cell Biology* 9:1233–1242. DOI: <https://doi.org/10.1038/ncb1643>, PMID: 17934454
- Yang G, Cameron LA, Maddox PS, Salmon ED, Danuser G. 2008. Regional variation of microtubule flux reveals microtubule organization in the metaphase meiotic spindle. *The Journal of Cell Biology* 182:631–639. DOI: <https://doi.org/10.1083/jcb.200801105>, PMID: 18710922
- Yu CH, Redemann S, Wu HY, Kiewisz R, Yoo TY, Conway W, Farhadifar R, Müller-Reichert T, Needleman D, Zheng Y. 2019. Central-spindle microtubules are strongly coupled to chromosomes during both anaphase A and anaphase B. *Molecular Biology of the Cell* 30:2503–2514. DOI: <https://doi.org/10.1091/mbc.E19-01-0074>, PMID: 31339442
- Xie, J. *et al.* Contribution of cytoplasm viscoelastic properties to mitotic spindle positioning. *Proceedings of the National Academy of Sciences* **119**, e2115593119 (2022).
- Zhai, Y., Kronebusch, P. J. & Borisy, G. G. Kinetochore microtubule dynamics and the metaphase-anaphase transition. *J Cell Biol* **131**, 721–734 (1995).

Publishing Agreement

It is the policy of the University to encourage open access and broad distribution of all theses, dissertations, and manuscripts. The Graduate Division will facilitate the distribution of UCSF theses, dissertations, and manuscripts to the UCSF Library for open access and distribution. UCSF will make such theses, dissertations, and manuscripts accessible to the public and will take reasonable steps to preserve these works in perpetuity.

I hereby grant the non-exclusive, perpetual right to The Regents of the University of California to reproduce, publicly display, distribute, preserve, and publish copies of my thesis, dissertation, or manuscript in any form or media, now existing or later derived, including access online for teaching, research, and public service purposes.

DocuSigned by:

C2DE4B8B0DB24A7... Author Signature

5/29/2024
Date